

Gaia Data Release 3: Reflectance spectra of Solar System small bodies ^{*}

Gaia Collaboration, L. Galluccio¹, M. Delbo¹, F. De Angeli², T. Pauwels³, P. Tanga¹, F. Mignard¹, A. Cellino⁴, A.G.A. Brown⁵, K. Muinonen^{6,7}, A. Penttilä⁶, S. Jordan⁸, A. Vallenari⁹, T. Prusti¹⁰, J.H.J. de Bruijne¹⁰, F. Arenou¹¹, C. Babusiaux^{12,11}, M. Biermann⁸, O.L. Creevey¹, C. Ducourant¹³, D.W. Evans², L. Eyer¹⁴, R. Guerra¹⁵, A. Hutton¹⁶, C. Jordi¹⁷, S.A. Klioner¹⁸, U.L. Lammers¹⁵, L. Lindegren¹⁹, X. Luri¹⁷, C. Panem²⁰, D. Pourbaix^{†21,22}, S. Randich²³, P. Sartoretti¹¹, C. Soubiran¹³, N.A. Walton², C.A.L. Bailer-Jones²⁴, U. Bastian⁸, R. Drimmel⁴, F. Jansen²⁵, D. Katz¹¹, M.G. Lattanzi^{4,26}, F. van Leeuwen², J. Bakker¹⁵, C. Cacciari²⁷, J. Castañeda²⁸, C. Fabricius¹⁷, M. Fouesneau²⁴, Y. Frémat³, A. Guerrier²⁰, U. Heiter²⁹, E. Masana¹⁷, R. Messineo³⁰, N. Mowlavi¹⁴, C. Nicolas²⁰, K. Nienartowicz^{31,32}, F. Pailler²⁰, P. Panuzzo¹¹, F. Riclet²⁰, W. Roux²⁰, G.M. Seabroke³³, R. Sordo⁹, F. Thévenin¹, G. Gracia-Abril^{34,8}, J. Portell¹⁷, D. Teyssier³⁵, M. Altmann^{8,36}, R. Andrae²⁴, M. Audard^{14,32}, I. Bellas-Velidis³⁷, K. Benson³³, J. Berthier³⁸, R. Blomme³, P.W. Burgess², D. Busonero⁴, G. Busso², H. Cánovas³⁵, B. Carry¹, N. Cheek³⁹, G. Clementini²⁷, Y. Damerджи^{40,41}, M. Davidson⁴², P. de Teodoro¹⁵, M. Nuñez Campos¹⁶, L. Delchambre⁴⁰, A. Dell’Oro²³, P. Esquej⁴³, J. Fernández-Hernández⁴⁴, E. Fraile⁴³, D. Garabato⁴⁵, P. García-Lario¹⁵, E. Gosset^{40,22}, R. Haigron¹¹, J.-L. Halbwachs⁴⁶, N.C. Hambly⁴², D.L. Harrison^{2,47}, J. Hernández¹⁵, D. Hestroffer³⁸, S.T. Hodgkin², B. Holl^{14,32}, K. Janßen⁴⁸, G. Jevardat de Fombelle¹⁴, A. Krone-Martins^{49,50}, A.C. Lanzafame^{51,52}, W. Löffler⁸, O. Marchal⁴⁶, P.M. Marrese^{53,54}, A. Moitinho⁴⁹, P. Osborne², E. Pancino^{23,54}, A. Recio-Blanco¹, C. Reylé⁵⁵, M. Riello², L. Rimoldini³², T. Roegiers⁵⁶, J. Rybizki²⁴, L.M. Sarro⁵⁷, C. Siopis²¹, M. Smith³³, A. Sozzetti⁴, E. Utrilla¹⁶, M. van Leeuwen², U. Abbas⁴, P. Abraham^{58,59}, A. Abreu Aramburu⁴⁴, C. Aerts^{60,61,24}, J.J. Aguado⁵⁷, M. Ajaj¹¹, F. Aldea-Montero¹⁵, G. Altavilla^{53,54}, M.A. Álvarez⁴⁵, J. Alves⁶², R.I. Anderson⁶³, E. Anglada Varela⁴⁴, T. Antoja¹⁷, D. Baines³⁵, S.G. Baker³³, L. Balaguer-Núñez¹⁷, E. Balbinot⁶⁴, Z. Balog^{8,24}, C. Barache³⁶, D. Barbato^{14,4}, M. Barros⁴⁹, M.A. Barstow⁶⁵, S. Bartolomé¹⁷, J.-L. Bassilana⁶⁶, N. Bauchet¹¹, U. Becciani⁵¹, M. Bellazzini²⁷, A. Berihuete⁶⁷, M. Bernet¹⁷, S. Bertone^{68,69,4}, L. Bianchi⁷⁰, A. Binnenfeld⁷¹, S. Blanco-Cuaresma⁷², T. Boch⁴⁶, A. Bombrun⁷³, D. Bossini⁷⁴, S. Bouquillon^{36,75}, A. Bragaglia²⁷, L. Bramante³⁰, E. Breedt², A. Bressan⁷⁶, N. Brouillet¹³, E. Brugaletta⁵¹, B. Bucciarelli^{4,26}, A. Burlacu⁷⁷, A.G. Butkevich⁴, R. Buzzì⁴, E. Caffau¹¹, R. Cancelliere⁷⁸, T. Cantat-Gaudin^{17,24}, R. Carballo⁷⁹, T. Carlucci³⁶, M.I. Carnerero⁴, J.M. Carrasco¹⁷, L. Casamiquela^{13,11}, M. Castellani⁵³, A. Castro-Ginard⁵, L. Chaoul²⁰, P. Charlot¹³, L. Chemin⁸⁰, V. Chiaramida³⁰, A. Chiavassa¹, N. Chornay², G. Comoretto^{35,81}, G. Contursi¹, W.J. Cooper^{82,4}, T. Cornez⁶⁶, S. Cowell², F. Crifo¹¹, M. Cropper³³, M. Crosta^{4,83}, C. Crowley⁷³, C. Dafonte⁴⁵, A. Dapergolas³⁷, P. David³⁸, P. de Laverny¹, F. De Luise⁸⁴, R. De March³⁰, J. De Ridder⁶⁰, R. de Souza⁸⁵, A. de Torres⁷³, E.F. del Peloso⁸, E. del Pozo¹⁶, A. Delgado⁴³, J.-B. Delisle¹⁴, C. Demouchy⁸⁶, T.E. Dharmawardena²⁴, S. Diakite⁸⁷, C. Diener², E. Distefano⁵¹, C. Dolding³³, H. Enke⁴⁸, C. Fabre⁸⁸, M. Fabrizio^{53,54}, S. Faigler⁸⁹, G. Fedorets^{6,90}, P. Fernique^{46,91}, F. Figueras¹⁷, Y. Fournier⁴⁸, C. Fouron⁷⁷, F. Fragkoudi^{92,93,94}, M. Gai⁴, A. Garcia-Gutierrez¹⁷, M. Garcia-Reinaldos¹⁵, M. García-Torres⁹⁵, A. Garofalo²⁷, A. Gavel²⁹, P. Gavras⁴³, E. Gerlach¹⁸, R. Geyer¹⁸, P. Giacobbe⁴, G. Gilmore², S. Girona⁹⁶, G. Giuffrida⁵³, R. Gomel⁸⁹, A. Gomez⁴⁵, J. González-Núñez^{39,97}, I. González-Santamaría⁴⁵, J.J. González-Vidal¹⁷, M. Granvik^{6,98}, P. Guillout⁴⁶, J. Guiraud²⁰, R. Gutiérrez-Sánchez³⁵, L.P. Guy^{32,99}, D. Hatzidimitriou^{100,37}, M. Hauser^{24,101}, M. Haywood¹¹, A. Helmer⁶⁶, A. Helmi⁶⁴, M.H. Sarmiento¹⁶, S.L. Hidalgo^{102,103}, N. Hładczuk^{15,104}, D. Hobbs¹⁹, G. Holland², H.E. Huckle³³, K. Jardine¹⁰⁵, G. Jasiewicz¹⁰⁶, A. Jean-Antoine Piccolo²⁰, Ó. Jiménez-Arranz¹⁷, J. Juaristi Campillo⁸, F. Julbe¹⁷, L. Karbevská^{32,107}, P. Kervella¹⁰⁸, S. Khanna^{64,4}, G. Kordopatis¹, A.J. Korn²⁹, Á Kóspál^{58,24,59}, Z. Kostrzewa-Rutkowska^{5,109}, K. Kruszyńska¹¹⁰, M. Kun⁵⁸, P. Laizeau¹¹¹, S. Lambert³⁶, A.F. Lanza⁵¹, Y. Lasne⁶⁶, J.-F. Le Campion¹³, Y. Lebreton^{108,112}, T. Lebzelter⁶², S. Leccia¹¹³, N. Leclerc¹¹, I. Lecoœur-Taïbi³², S. Liao^{114,4,115}, E.L. Licata⁴, H.E.P. Lindstrøm^{4,116,117}, T.A. Lister¹¹⁸, E. Livanou¹⁰⁰, A. Lobel³, A. Lorca¹⁶, C. Loup⁴⁶, P. Madrero Pardo¹⁷, A. Magdaleno Romeo⁷⁷, S. Managau⁶⁶, R.G. Mann⁴²,

M. Manteiga¹¹⁹, J.M. Marchant¹²⁰, M. Marconi¹¹³, J. Marcos³⁵, M.M.S. Marcos Santos³⁹, D. Marín Pina¹⁷, S. Marinoni^{53,54}, F. Marocco¹²¹, D.J. Marshall¹²², L. Martin Polo³⁹, J.M. Martín-Fleitas¹⁶, G. Marton⁵⁸, N. Mary⁶⁶, A. Masip¹⁷, D. Massari²⁷, A. Mastrobuono-Battisti¹¹, T. Mazeh⁸⁹, P.J. McMillan¹⁹, S. Messina⁵¹, D. Michalik¹⁰, N.R. Millar², A. Mints⁴⁸, D. Molina¹⁷, R. Molinaro¹¹³, L. Molnár^{58,123,59}, G. Monari⁴⁶, M. Monguió¹⁷, P. Montegriffo²⁷, A. Montero¹⁶, R. Mor¹⁷, A. Mora¹⁶, R. Morbidelli⁴, T. Morel⁴⁰, D. Morris⁴², T. Muraveva²⁷, C.P. Murphy¹⁵, I. Musella¹¹³, Z. Nagy⁵⁸, L. Noval⁶⁶, F. Ocaña^{35,124}, A. Ogden², C. Ordenovic¹, J.O. Osinde⁴³, C. Pagani⁶⁵, I. Pagano⁵¹, L. Palaversa^{125,2}, P.A. Palicio¹, L. Pallas-Quintela⁴⁵, A. Panahi⁸⁹, S. Payne-Wardenaar⁸, X. Peñalosa Esteller¹⁷, J.-M. Petit⁵⁵, B. Pichon¹, A.M. Piersimoni⁸⁴, F.-X. Pineau⁴⁶, E. Plachy^{58,123,59}, G. Plum¹¹, E. Poggio^{1,4}, A. Prša¹²⁶, L. Pulone⁵³, E. Racero^{39,124}, S. Ragaini²⁷, M. Rainer^{23,127}, C.M. Raiteri⁴, P. Ramos^{17,46}, M. Ramos-Lerate³⁵, P. Re Fiorentin⁴, S. Regibo⁶⁰, P.J. Richards¹²⁸, C. Rios Diaz⁴³, V. Ripepi¹¹³, A. Riva⁴, H.-W. Rix²⁴, G. Rixon², N. Robichon¹¹, A.C. Robin⁵⁵, C. Robin⁶⁶, M. Roelens¹⁴, H.R.O. Rogues⁸⁶, L. Rohrbasser³², M. Romero-Gómez¹⁷, N. Rowell⁴², F. Royer¹¹, D. Ruz Mieres², K.A. Rybicki¹¹⁰, G. Sadowski²¹, A. Sáez Núñez¹⁷, A. Sagristà Sellés⁸, J. Sahlmann⁴³, E. Salguero⁴⁴, N. Samaras^{3,129}, V. Sanchez Gimenez¹⁷, N. Sanna²³, R. Santoveña⁴⁵, M. Sarasso⁴, M. Schultheis¹, E. Sciacca⁵¹, M. Segol⁸⁶, J.C. Segovia³⁹, D. Ségransan¹⁴, D. Semeux⁸⁸, S. Shahaf¹³⁰, H.I. Siddiqui¹³¹, A. Siebert^{46,91}, L. Siltala⁶, A. Silvelo⁴⁵, E. Slezak¹, I. Slezak¹, R.L. Smart⁴, O.N. Snaith¹¹, E. Solano¹³², F. Solitro³⁰, D. Souami^{108,133}, J. Souchay³⁶, A. Spagna⁴, L. Spina⁹, F. Spoto⁷², I.A. Steele¹²⁰, H. Steidelmüller¹⁸, C.A. Stephenson^{35,134}, M. Süveges¹³⁵, J. Surdej^{40,136}, L. Szabados⁵⁸, E. Szegedi-Elek⁵⁸, F. Taris³⁶, M.B. Taylor¹³⁷, R. Teixeira⁸⁵, L. Tolomei³⁰, N. Tonello⁹⁶, F. Torra²⁸, J. Torra¹⁷, G. Torralba Elipe⁴⁵, M. Trabucchi^{138,14}, A.T. Tsounis¹³⁹, C. Turon¹¹, A. Ulla¹⁴⁰, N. Unger¹⁴, M.V. Vaillant⁶⁶, E. van Dillen⁸⁶, W. van Reeve¹⁴¹, O. Vanel¹¹, A. Vecchiato⁴, Y. Viala¹¹, D. Vicente⁹⁶, S. Voutsinas⁴², M. Weiler¹⁷, T. Wevers^{2,142}, Ł. Wyrzykowski¹¹⁰, A. Yoldas², P. Yvard⁸⁶, H. Zhao¹, J. Zorec¹⁴³, S. Zucker⁷¹, and T. Zwitter¹⁴⁴

(Affiliations can be found after the references)

ABSTRACT

Context. The *Gaia* mission of the European Space Agency (ESA) has been routinely observing Solar System objects (SSOs) since the beginning of its operations in August 2014. The *Gaia* data release three (DR3) includes, for the first time, the mean reflectance spectra of a selected sample of 60 518 SSOs, primarily asteroids, observed between August 5, 2014, and May 28, 2017. Each reflectance spectrum was derived from measurements obtained by means of the Blue and Red photometers (BP/RP), which were binned in 16 discrete wavelength bands. For every spectrum, the DR3 also contains additional information about the data quality for each band.

Aims. We describe the processing of the *Gaia* spectral data of SSOs, explaining both the criteria used to select the subset of asteroid spectra published in *Gaia* DR3, and the different steps of our internal validation procedures. In order to further assess the quality of *Gaia* SSO reflectance spectra, we carried out external validation against SSO reflectance spectra obtained from ground-based and space-borne telescopes and available in the literature; we present our validation approach.

Methods. For each selected SSO, an epoch reflectance was computed by dividing the calibrated spectrum observed by the BP/RP at each transit on the focal plane by the mean spectrum of a solar analogue. The latter was obtained by averaging the *Gaia* spectral measurements of a selected sample of stars known to have very similar spectra to that of the Sun. Finally, a mean of the epoch reflectance spectra was calculated in 16 spectral bands for each SSO.

Results. *Gaia* SSO reflectance spectra are in general agreement with those obtained from a ground-based spectroscopic campaign specifically designed to cover the same spectral interval as *Gaia* and mimic the illumination and observing geometry characterising *Gaia* SSO observations. In addition, the agreement between *Gaia* mean reflectance spectra and those available in the literature is good for bright SSOs, regardless of their taxonomic spectral class. We identify an increase in the spectral slope of S-type SSOs with increasing phase angle. Moreover, we show that the spectral slope increases and the depth of the 1 μm absorption band decreases for increasing ages of S-type asteroid families. The latter can be interpreted as proof of progressive ageing of S-type asteroid surfaces due to their exposure to space weathering effects.

Key words. spectrophotometry – minor planets, asteroids: general – methods: data analysis – space vehicles: instruments

1. Introduction

A major breakthrough of the last several decades in astrophysics has been the discovery of the great diversity of planetary systems in our Galaxy and their marked differences with respect to

our Solar System (Winn & Fabrycky 2015). This observational progress has boosted research in one of the oldest subjects of planetary science, namely understanding the formation of planets and their evolution (Morbidelli & Raymond 2016; Raymond et al. 2020). How discs of dust and gas around similar stars evolved and eventually led to the great planetary diversity that we observe and why our own Solar System took a path that is uncommon amongst others are fundamental questions of planetary science and astrophysics.

* This article is dedicated to the memory of Dimitri Pourbaix, who laid the foundations and directed the Coordination Unit 4 (CU4) of the Data Processing and Analysis Consortium (DPAC) of the ESA mission *Gaia*.

Studying the Solar System objects (SSOs) is key to answering the above questions. For instance, the current orbital structure of asteroids informs us about dynamical events that the planets of our Solar System have undergone during their formation and evolution (Minton & Malhotra 2009; Walsh et al. 2011; Raymond & Izidoro 2017; Nesvorný 2018; Raymond & Nesvorný 2020). One of these events was a brief and violent phase of orbital instability of the giant planets (Tsiganis et al. 2005; Nesvorný & Morbidelli 2012). In addition, asteroids contain material that is the most pristine of all the material dating back to the formation of our Solar System 4.5 billion of years ago (see the review of Libourel et al. 2017, and references therein). Moreover, some asteroids are the parent bodies of the meteorites, which are a major source of information about the evolution of the material in the protoplanetary disc (Zolensky et al. 2006).

The largest repository of asteroids is the main belt, which comprises bodies with stable orbits between Mars and Jupiter. However, over time, collisions have shattered some of these asteroids, creating families of fragments; these have drifted along the orbital semi-major axis (due to a non-gravitational force known as the Yarkovsky effect; Vokrouhlický & Farinella 2000; Bottke et al. 2000; Rubincam 2000; Bottke et al. 2006) until reaching orbital instability zones capable of increasing orbital eccentricity, causing these asteroid fragments to cross the orbits of the inner planets (Morbidelli & Vokrouhlický 2003; Granvik et al. 2017, 2018). Close encounters with planets can fully change the orbits of these bodies to be in the terrestrial planet region. Because these near-Earth asteroids can impact our planet, substantial effort has been devoted to the studying their population (Mainzer et al. 2011, 2015; Morbidelli et al. 2020), in some cases in order to assess impact hazard (Michel 2013).

More recently, asteroids have been targeted by space missions of Solar System exploration. Several missions flew by or rendezvoused with asteroids, such as (951) Gaspra (Belton et al. 1992), (243) Ida (Belton et al. 1995), (253) Mathilde (Veverka et al. 1996), (433) Eros (Veverka et al. 2000), (25143) Itokawa (Abe et al. 2006), (2867) Šteins (Keller et al. 2010), (21) Lutetia (Sierks et al. 2011), (4) Vesta (Reddy et al. 2012), (4179) Toutatis (Huang et al. 2013), (1) Ceres (Russell et al. 2004), (162173) Ryugu (Sugita et al. 2019), and (101955) Bennu (Laurtta et al. 2019). These visits revealed a great variety in the composition and nature of the surfaces of these objects. More missions are flying towards asteroids, such as NASA's Lucy, which is bound to explore the Jupiter Trojan asteroids (Olkin et al. 2021), and the NASA Double Asteroid Redirection Test (DART), which plans to impact the natural satellite of the double asteroid (65803) Didymos (Rivkin et al. 2021). In August 2022, NASA will also launch the Psyche mission to explore the main-belt asteroid (16) Psyche, which is thought to be a remnant of the metallic core of a disrupted planetesimal (Elkins-Tanton et al. 2016). Furthermore, in 2024, ESA will launch Hera to investigate the Didymos binary asteroid, including the very first assessment of its internal properties, and to measure the outcome of the DART mission kinetic impactor test (Michel et al. 2021).

Given all of the above, determining the composition of asteroids is of utmost importance. Most of the data collected so far have been collected from the ground using different techniques, including spectroscopy, photometry, polarimetry, radar experiments, and adaptive optics imaging. Spectroscopy is the preferred method to estimate asteroid surface composition from the wavelength dependent reflectance of the surface (see Bus et al. 2002, for a review). The observed diversity of the reflectance spectra of asteroids has been traditionally used to develop taxonomic classifications (see DeMeo et al. 2015, for a re-

view). These taxonomic classes express the relative abundances of asteroids across the Solar System (Gradie & Tedesco 1982; Gradie et al. 1989) and their mixing (DeMeo & Carry 2014). Reflectance spectra are also typically used to link meteorites to their parent asteroids (e.g. Popescu et al. 2016; DeMeo et al. 2022). These links are extremely useful for relating detailed laboratory measurements to the orbital distribution and classes of small bodies.

The existence of different classes of asteroids is interpreted by many authors in terms of a variety of surface compositions likely resulting from differences in origin and evolution. The different orbital distributions of distinct taxonomic classes are believed to be diagnostic of phenomena of early mixing of different classes of planetesimals across the Solar System (Gradie & Tedesco 1982; Gradie et al. 1989; DeMeo & Carry 2014), and provide an important input for theoretical models of the early phases of evolution of our planetary system (Gomes et al. 2005; Pierens et al. 2014; Walsh et al. 2012).

In this context, it is very important to be able to disentangle properties due to the early history of the Solar System from those resulting from long-term evolution beginning from when the current structure of the Solar System was attained. The knowledge accumulated over decades of investigations suggests that there are essentially three physical processes that play a major role in the evolution of the asteroid population. The first is collisional evolution, which progressively affects the inventory and size distribution of the main belt asteroids, and their surfaces; for example by producing craters (Davis et al. 1979; Farinella et al. 1981, 1992; Davis et al. 1985, 2002; Morbidelli et al. 2009; Bottke et al. 2015). The second is space weathering. This is due to the exposure of asteroid surfaces to irradiation from cosmic rays, solar wind, and collisions with micro-meteorites. For decades, we have known that space weathering progressively modifies the reflectance spectra of asteroids, the most important effects having been found to affect the class of asteroids belonging to the so-called S-complex, which includes objects believed to be the parent bodies of the most common class of meteorites, the ordinary chondrites (Brunetto et al. 2006). The third is the realisation that the simple cycle of thermal expansion and contraction of the material constituting the outer layer of surface regolith, which is due to rotation of the body, leads to progressive evolution of the regolith structural and thermal properties (Delbo et al. 2014; Molaro et al. 2017, 2020). Of course, there is interplay between the above-mentioned evolution mechanisms. For instance, energetic collisions not only generate families, producing the exposure of the internal layers of their parent bodies, but also restart the space weathering clock and trigger a Yarkovsky-driven dynamical evolution of the smallest fragments.

Spectrophotometry has been a very important tool for understanding the compositional big picture of the asteroid population. Initiated in the 1980s with the Eight Color Asteroid Survey (ECAS, Zellner et al. 1985), spectrophotometric asteroid surveys evolved with the 24-colour asteroid survey (Chapman et al. 2005), the 52-colour survey (Bell et al. 1988), the Seven Colour Asteroid Survey in the infrared (Clark et al. 1993), the moving object component of the Sloan digital sky survey (SDSS) (Ivezić et al. 2019), which in its latest analysis provided measurements for 379 714 known asteroids (Sergeyev & Carry 2021). Moreover, we recall the near-infrared (NIR) colours of asteroids recovered from the Visible and Infrared Survey Telescope for Astronomy - VISTA Hemisphere Survey (VISTA-VHS) and the Moving Objects from VISTA survey (MOVIS; Popescu et al. 2016), the Korea Microlensing Telescope Network-South African Astronomical Observatory (KMTNET-SAAO) Multi-

band Photometry survey (Erasmus et al. 2019), the moving object observations from the Javalambre Photometric Local Universe Survey (J-PLUS) (Morate et al. 2021), and the multi-filter photometry of Solar System objects from the SkyMapper Southern Survey (Sergeyev et al. 2022). In total, over 1.5 million spectrophotometric observations of asteroids exist.

Among several spectroscopic surveys of small bodies carried out by different authors, we mention the SMall Asteroid Spectroscopic Survey of the MIT in the visible light (SMASS) phase I (Xu et al. 1995), II (Bus & Binzel 2002a,b), and in the NIR (Burbine & Binzel 2002); the MIT-Hawaii Near-Earth Object Spectroscopic Survey (MITHNEOS, Binzel et al. 2019; Marsset et al. 2022); the Small Solar System Objects Spectroscopic Survey (S^3OS^2) (Lazzaro et al. 2004b); the Mission Accessible Near-Earth Objects Survey (MANOS) of the Lowell Observatory (Devogèle et al. 2019); the PRIMitive Asteroids Spectroscopic Survey (PRIMASS, de Leon et al. 2018); and efforts devoted to the characterisation of small near-Earth objects (Perna et al. 2018a). In the literature, more than 7600 asteroid spectra are available today. We note that the most modern asteroid spectroscopic surveys covered preferentially the visible and NIR spectral regions, whereas the blue region has been lost downward of about 450-500 nm in many cases. This makes an interesting difference with the reflectance spectra obtained by *Gaia*, as explained below.

It is in this framework that here we present the survey of reflectance spectra of 60 518 Solar System small bodies contained in the Data Release 3 (DR3) of the ESA mission *Gaia*. Successfully launched from Kourou spaceport, French Guiana, on 19 December 2013, *Gaia* started its nominal mission on 25 July 2014; it continuously observed celestial bodies, including SSOs, with magnitudes ≤ 21 entering the field of view according to a predefined (so-called nominal) sky scanning law (Gaia Collaboration et al. 2016). The detectors on the focal plane of *Gaia*, which is optimised for achieving unprecedented astrometric accuracy, include two low-resolution slit-less spectrographs capable of providing SSO spectroscopy. One of them is optimised for observations in the blue region of the visible light and is called Blue-Photometer (BP), while the other is optimised for the red region and is called Red-Photometer (RP). Both spectrographs are sometimes collectively referred to herein as XP.

The *Gaia* DR3 is the largest space-based survey of asteroid reflectance spectrophotometry in the visible range to date. *Gaia* DR3 contains averaged spectra of main belt asteroids (MBAs), near-Earth asteroids (NEAs), Centaurs, Jupiter Trojans, and a few transneptunian objects (TNOs) (see Table 1). For each SSO, one reflectance spectrum sampled in 16 wavelength bands is provided. This is the result of averaging several epoch reflectance spectra. While the DR3 also contains astrometry and photometry of 158 152 SSOs (Tanga 2022), it does not contain epoch spectra, nor spectra of natural satellites or comets. The publication of these are foreseen for later releases.

Gaia SSO reflectance spectra will be complementary to spectrophotometric data that are expected from the ESA Euclid mission, which will observe several tens of thousand of asteroids in three wide wavelength bands covering the near-infrared region of the electromagnetic spectrum (Carry 2018). In addition, at the end of 2022, the Large Synoptic Survey Telescope (LSST) of the Vera Rubin Observatory will be commissioned and will begin operations. Approximately two years later, the LSST teams will start publishing the fully calibrated spectrophotometric data. In a single visit, LSST is expected to be able to detect up to 5000 Solar System objects. Over its ten-year nominal lifespan, LSST could catalogue over 5 million MBAs, almost 300,000 Jupiter

Trojans, over 100,000 NEAs, and over 40,000 TNOs. Many of these objects will be observed hundreds of times in six broad bands from 0.35 to 1.1 microns (LSST Science Collaboration et al. 2009; Ivezić et al. 2019; Vera C. Rubin Observatory LSST Solar System Science Collaboration et al. 2020). *Gaia* spectroscopic data of SSOs will offer a key comparison against LSST spectrophotometry, allowing us to study the biases of both surveys and also the potential time spectral variability of asteroids.

This article is organised as follows: in section 2, we present *Gaia* observations, in section 3, we describe the methods used to create the SSO reflectance spectrophotometry, and in section 4, we present our validation of SSO reflectances. In section 5, we discuss our main results.

2. Observations

Observations that resulted in the DR3 data were collected by *Gaia* during the nominal mission operations from Earth's Lagrangian Point L2 between 5 August 2014 and 28 May 2017. We processed 158 152 SSOs (see Tanga 2022, for a complete description on their selection and their complete processing). However, not all these observations resulted in usable reflectance spectra. Figures 1 and 2 show the orbital distribution and the mean value of the G magnitude, respectively, of the 60 518 SSOs that have a valid mean reflectance spectrum in the DR3. This shows that the majority of these SSOs have been observed with magnitudes of between ~ 18 and 20. The faintest SSO with *Gaia* DR3 spectrophotometry is asteroid 2004 RH₃₁₉, which was observed with a mean G magnitude of 20.19. Table 1 presents the number of SSOs with DR3 reflectance spectra for each dynamical class. These dynamical classes are listed at the NASA Jet Propulsion Laboratory web site ¹.

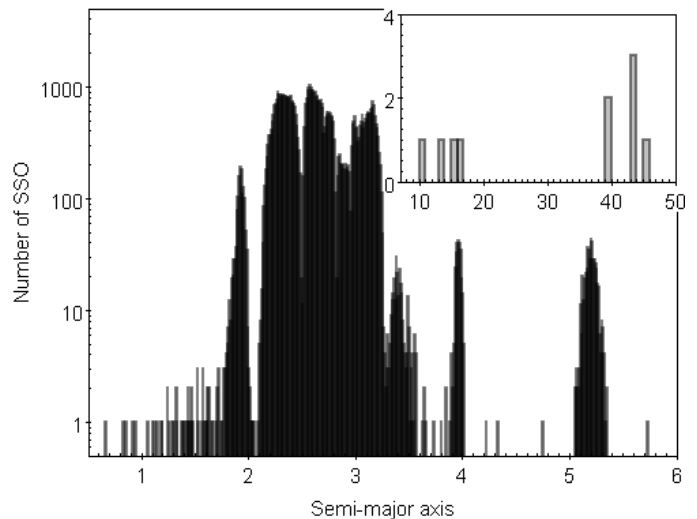


Fig. 1. Orbital distribution of SSOs with reflectance spectra in *Gaia* DR3.

The *Gaia* satellite is equipped with two telescopes that collect the light of astronomical sources on a shared focal plane composed of 106 charge-coupled device (CCD) detectors. Due to the rotation of *Gaia*, the sources move on the focal plane and encounter a series of different instruments. The first are the SkyMapper (SM) instruments that are used by the on-board electronics to detect the sources. The light is then measured by each of the nine astrometric field (AF) CCDs. Next, it is dispersed

¹ https://ssd.jpl.nasa.gov/tools/sbdb_query.html

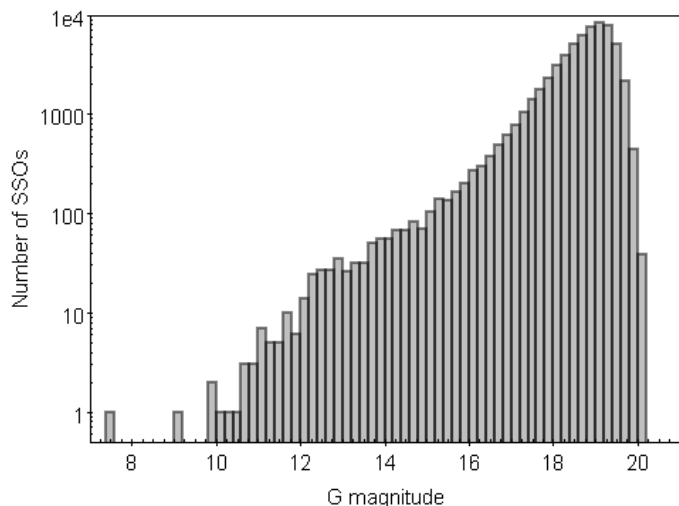


Fig. 2. G-magnitude distribution of SSOs with reflectance spectra.

Table 1. Number (No.) of SSOs with *Gaia* DR3 spectra for each of the dynamical classes listed on the NASA JPL website. The classes are defined according to criteria based on the orbital semimajor axis, a , the perihelion distance, q , and the aphelion distance, Q .

Dynamical class	No. of SSO	Criterion (values in au)
NEA Aten	6	$a < 1.0$ & $Q > 0.983$
NEA Apollo	52	$a > 1.0$ & $q < 1.017$
NEA Amor	47	$1.017 < q < 1.3$
Mars-Crosser	729	$1.3 < q < 1.666$
Inner Main Belt	1 221	$a < 2.0$ & $q > 1.666$
Main Belt	55 976	$2.0 < a < 3.2$ & $q > 1.666$
Outer Main Belt	1 995	$3.2 < a < 4.6$
Jupiter Trojan	477	$4.6 < a < 5.5$
Centaur	5	$5.5 < a < 30.1$
TNO	7	$a > 30.1$
Other	2	none of the above

by the two slit-less prisms and collected by the XP instruments (for the instrument layout, see Jordi et al. 2010, in particular their Figure 2). On each XP, the on-board electronics consider only a small window of 60×12 pixels (along scan, AL, \times across scan, AC; the angular size of an AL pixel is 58.933 milli-arcsec) centred on each spectrum. This window is also binned in the AC direction in order to compose a 1D spectrum of 60 samples. Among these, in general, only the 40 central pixels contain exploitable signal. The edges of the windows are mainly dominated by the background and the extended wings of the line spread function (LSF; Carrasco et al. 2021). One spectrum per XP is produced. The BP operates in the wavelength range between 330 and 680 nm, while the RP in the range between 640 and 1050 nm (see Appendix A for the spectral resolution of each spectrophotometer).

Due to the *Gaia* scanning law of the sky, SSOs are never observed at opposition. Figure 3 presents the histogram of the average phase angles (the Sun-SSO-*Gaia* angle) of SSO spectroscopic observations. For each SSO, this is calculated as the straight arithmetic average of the phase angles of the observations producing valid epoch reflectance spectra. Most of the MBAs are observed by *Gaia* with a phase angle of around 20 degrees. However, Jupiter Trojans, Centaurs, and TNOs are in general observed with lower phase angles than MBAs.

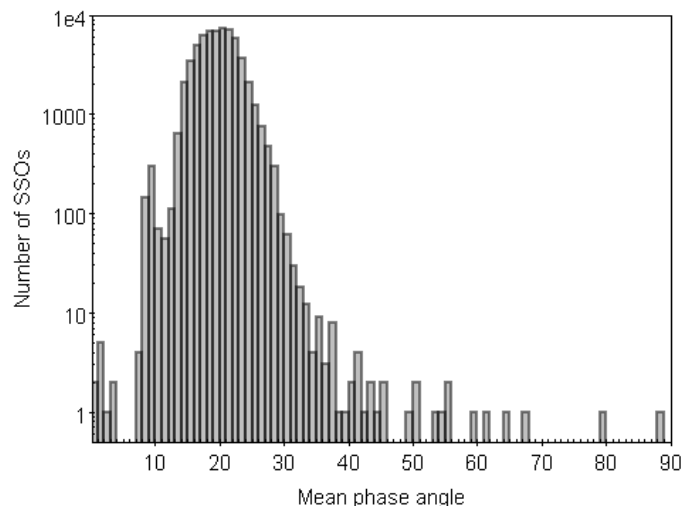


Fig. 3. Phase angle distribution of SSOs with reflectance spectra. For each SSO, only the phase angles of the transits used to compute the mean reflectance spectrum are averaged and contribute to the plot.

Each SSO is typically observed at multiple epochs, typically 60 times during the nominal five-year duration of the mission (Tanga & Mignard 2012, however, the *Gaia* mission has been extended). Each epoch corresponds to a transit of the SSO on the *Gaia* focal plane, and receives a unique identifier called *transit_id*. However, not all observations obtained by *Gaia* eventually produce an exploitable epoch spectrum. Several factors can affect the production of spectra, as in the case where a window is affected by multiple peaks, a charge injection, a gate release, a satellite event, and so on. Some issues can also happen during the calibration of the spectrum; for example, a poor prediction of the source position might lower the quality of the spectrum. In the case of *Gaia* DR3, we found that almost 80% of the epoch spectra for each SSO produced by the spectrophotometric pipeline PhotPipe (see below) could be used to compute the mean reflectance spectra.

3. Data processing

The process that leads to the generation of internally calibrated BP/RP spectra (Carrasco et al. 2021; De Angeli et al. 2022) converts the observed raw pixel data into an internal system that is homogeneous across all different instrumental configurations. This is obtained by calibrating and removing a number of instrumental and astrophysical effects such as the CCD bias, background, geometry, differential dispersion, variations in response, and variation in the LSF across the focal plane. The main product of this process is a set of internally calibrated epoch spectra for each source and each epoch (i.e. transit on the focal plane). Internally calibrated epoch spectra are represented by arrays of 60×1 internal flux values and flux uncertainties, corresponding to the 60 pixel-long CCD windows on each XP. The 60 samples are given as a function of the so-called pseudo-wavelengths. Pseudo-wavelengths correspond to the wavelengths measured in units of sample in a reference location in the focal plane, before they are transformed into physical wavelength units (such as nanometers). This internal pseudo-wavelength scale provides homogeneity across all observations, while being close to the actual wavelength sampling of each XP instrument, which allows the alignment of observed spectra. For each source that is not a SSO (mainly stars), several internally calibrated epoch spectra

were aligned thanks to this pseudo-wavelength scale and then averaged over the epochs (transits) to produce so-called mean spectra. *Gaia* DR3 includes mean spectra for about 220 million sources. The mean spectra of a set of stars known to have a spectrum that is analogous to that of our Sun were extracted and averaged to produce a single solar analogue reference spectrum (see Appendix C).

However, due to the intrinsic variability and proper motion of SSOs, the calculation of their mean spectra was not performed. Instead, for each SSO and each epoch, the nominal, pre-launch dispersion function was used to convert pseudo-wavelengths to physical wavelengths. This procedure was complicated by the dispersed image formation in the time-delay integration (TDI) mode that is used by *Gaia*, whereby the dispersion function can only be defined in terms of a relation between wavelengths and the offset in the data space with respect to some reference point in the dispersed image.

This reference point is given by the prediction of the location of a given reference wavelength via the knowledge of the source position in the sky, the satellite attitude, and the geometry of the XP CCDs. For SSOs, data from the AF and predicted sky-plane motion of the SSO from the ephemerides were instead used to determine the field angles —namely the angular coordinates of the source on the focal plane— for each transit as a function of time (see Lindegren et al. 2012, in particular their Figure 2). The use of the ephemerides, rather than the estimate of the sky-plane motion that can be obtained from a single AF transit, allows us to obtain higher accuracy in the predictions of the aforementioned reference point. Three different epochs were used, namely 45, 50, and 55 seconds after the epoch of the read-out of the AF1 window. The latter is measured by *Gaia* on-board electronics and coded in the *transit_id*. These three epochs bracket the times of XP observations. The field angles at the exact observation time for the BP and the RP were then determined for each SSO transit by interpolation. The wavelength reference point was therefore determined, and the nominal dispersion function applied. This resulted in epoch spectra whose 60 flux and flux uncertainty samples were expressed in terms of physical wavelengths.

Subsequently, an epoch reflectance $R(\lambda_i)_t$ was determined by dividing the flux $f_i(\lambda_i)_t$ of each SSO epoch spectrum with *transit_id* t by the reference solar analogue spectrum $F(\lambda)$. The index i refers to the discrete samples of the epoch spectrum and can therefore take integer values between 0 and 59; λ_i is the corresponding physical wavelength. We note that $(\lambda_i)_t \neq (\lambda_i)_{t'}$ for $t \neq t'$ due to the different sampling of epoch spectra:

$$R(\lambda_i)_t = \frac{1}{\xi_t} \frac{f(\lambda_i)_t}{F(\lambda_i)}. \quad (1)$$

The ξ_t factor was defined to allow for normalisation of the epoch reflectance to 1 at 550 nm and was calculated as the mean reflectance value of samples with wavelength between 525 nm $\leq \lambda_i \leq 575$ nm:

$$\xi_t = \frac{1}{N} \sum_{\substack{i \leq i_{575} \\ i \geq i_{525}}} \frac{f(\lambda_i)_t}{F(\lambda_i)}, \quad (2)$$

where i_{525} and i_{575} denote the index range corresponding to the wavelength range of interest and N is the number of reflectance values being measured between 525 and 575 nm.

The uncertainty of ξ_t was computed as the standard error of the mean. We defined the sample standard deviation σ_{ξ_t} as

$$\sigma_{\xi_t} = \frac{1}{\sqrt{N-1}} \sqrt{\sum_{i=1}^N (R(\lambda_i)_t - \xi_t)^2}, \quad (3)$$

from which the standard error on the mean was computed as

$$\sigma_{\bar{\xi}_t} = \frac{\sigma_{\xi_t}}{\sqrt{N}}. \quad (4)$$

The uncertainty $\sigma(\lambda_i)_t$ on $R(\lambda_i)_t$ was calculated by propagating the uncertainties on $f(\lambda_i)_t$ and $F(\lambda)$ assuming them to be independent. The $R(\lambda_i)_t$ values were calculated separately for BP and RP, but the ξ_t factor was assumed to be the same for both BP and RP. Samples for which $R(\lambda_i)_t \leq 0$ or $\sigma(\lambda_i)_t > 1$ were rejected. Only BP and RP epoch reflectance samples corresponding to wavelengths in the ranges [325, 650] nm and [650, 1125] nm, respectively, were used to generate the mean reflectance spectra.

Visual inspection of the resulting epoch reflectances showed well-behaved continuous curves, with the exception of a few rare cases for some of the brightest SSOs, which display high spectral frequency variability. An extreme example of this rare problem is shown in Fig. 4.

In the large majority of cases, the BP and RP epoch reflectances

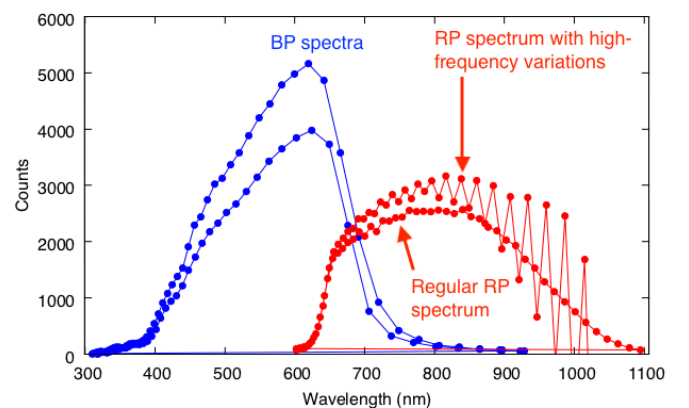


Fig. 4. Example of a regular epoch spectrum and of a spectrum whose RP part shows anomalous high-frequency variations. Epoch spectra are from the same main belt asteroid, (90) Antiope.

overlap in the wavelength range $650 \lesssim \lambda \lesssim 680$ nm covered by both instruments. However, in some rare cases, the superposition did not occur and the RP reflectance is lower, or higher, than the BP one (see Fig. 6). In order to avoid the degradation of the mean reflectance spectra because of this discrepancy, some filters described below were put in place.

In *Gaia* DR3, we present one mean reflectance spectrum, \bar{R} , per SSO. This mean reflectance is calculated by averaging $R(\lambda_i)_t$ over the set of epochs (or transits) t for each SSO. Figure 5 reports the number of epoch spectra per SSO used to compute the mean reflectance spectrum. The minimum number of epoch spectra per asteroid considered to allow the computation of the mean reflectance is three. The peak of the distribution is around 15. We expect an important increase in the number of epoch spectra per SSO for *Gaia* DR4 because of the increase in the number of observations by a factor of two and the improvements in the calibration process, which will lead to a decrease in the number of transits that we had to filter out for the current DR3.

The averaging of SSO epoch reflectances was performed as follows: firstly, we defined a set of fixed wavelengths λ_j every 44 nm in the range between 374 and 1034 nm. Next, we defined a set of wavelength bins 44 nm wide centred on each λ_j . Inside each wavelength bin, we calculated the weighted mean of the values of $R(\lambda_i)_t$ using $1/\sigma_{R(\lambda_i)_t}^2$ as weight. For each band, the median and the median absolute deviation (MAD) values were computed. A σ -clipping approach was used for filtering out all values

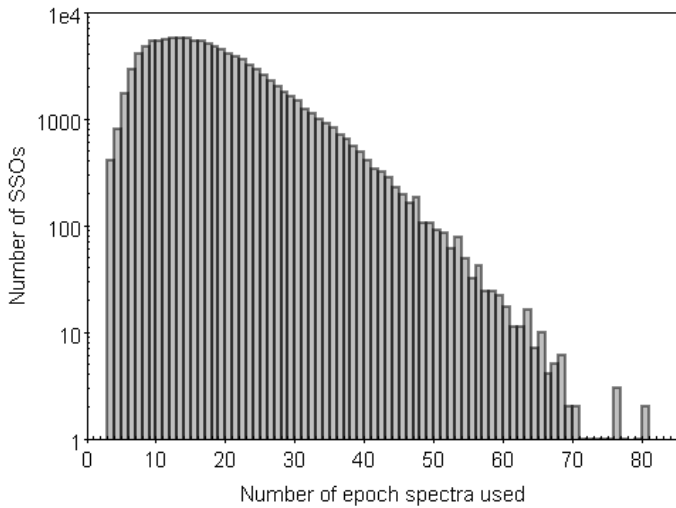


Fig. 5. Distribution of the number of epoch spectra used for the calculation of SSO mean reflectance spectra.

in each band that were outside the range ($\text{median}_{\lambda_i} - 2.5 \text{ MAD}$, $\text{median}_{\lambda_i} + 2.5 \text{ MAD}$); this was repeated twice in order to remove outliers.

A weighted average of each band was computed using the surviving epoch reflectance values:

$$\bar{R}(\lambda_i) = \frac{1}{\sum w_i} \sum w_i R(\lambda_i)_t. \quad (5)$$

Finally, all reflectances were normalised by the value at $\lambda = 550$ nm. Figure 6 shows the final result for one particular case.

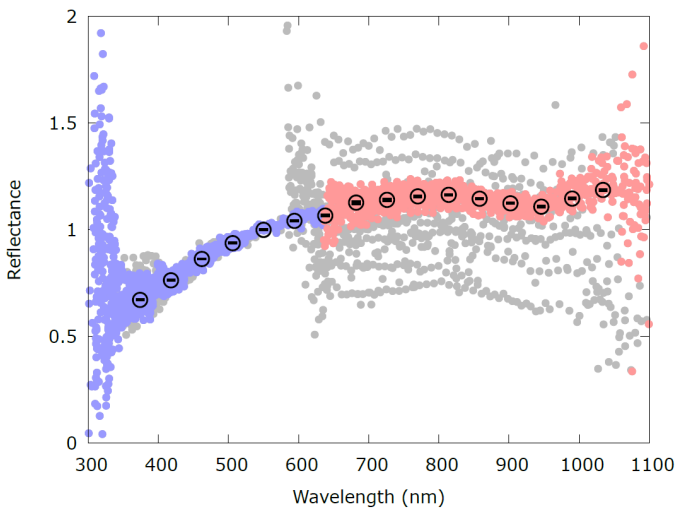


Fig. 6. Example of the mean computed reflectance $\bar{R}(\lambda_i)$ (black circles) for the asteroid (61) Danae. The grey points are the $R(\lambda_i)_t$, corresponding to each epoch reflectance. The $R(\lambda_i)_t$ values that are accepted by our filtering method are coloured in light blue (BP) and light red (RP).

The choice of the positioning of the 16 bands was dictated by two criteria: First, we required a whole band on a wavelength interval between 352 and 396 nm corresponding to an acceptable response of the BP. This has been verified on spectra with $S/N \geq 100$. Second, we needed to preserve a band centred at 550 nm to facilitate normalisation and comparison with literature data.

In order to clean up our catalogue of mean reflectance spectra from anomalous cases, we put in place a filtering procedure: we

determined the best-fit straight line to $\bar{R}(\lambda_i)_t$ in the range $450 \leq (\lambda_i)_t \leq 600$ nm; we used the straight line equation to calculate a value R_t^N at 550 nm and an extrapolated value of the R_t^E at 726 nm; we calculated a value of the mean reflectance R_t^M and of its standard deviation σ_t^M by averaging those values of $\bar{R}(\lambda_i)_t$ with $680 \leq (\lambda_i)_t \leq 780$ nm; we measured the discrepancy $\delta_t = |R_t^M - R_t^E|$; we rejected all values of $\bar{R}(\lambda_i)_t$ where $\delta_t \geq 0.30$ or $\sigma_t^M \geq 0.2$ or $\sum_i^{\text{BP}} \bar{R}(\lambda_i)_t \leq 0$ or $\sum_i^{\text{RP}} \bar{R}(\lambda_i)_t \leq 0$ or $|R_t^N - 1| \geq 0.15$. Figure 7 presents epoch and mean reflectance spectra computed for one typical SSO.

Apart from the bright asteroids, most of which have known spectra already, epoch spectra have quite low S/N. For *Gaia* DR3, the DPAC decided to provide the most reliable data, hence the mean reflectances. Epoch spectra will be published in future releases. This will allow us to (1) use improved mission calibrations (calibrations covering the entire mission are updated and improved for each release) and (2) have a larger number of epoch spectra per SSO, thus permitting a more reliable detection of outliers compared to the DR3.

4. Validation

Having produced the mean reflectance spectra, the next step was to assess their quality and compare them with external data. We performed this validation in three steps, which are presented in the subsections below.

4.1. Internal consistency and S/N threshold for publication

In Section 3, we described how the 16-band mean reflectance spectra were initially produced for 111 818 asteroids. However, visual inspection of some (thousands) of these spectra clearly showed that objects of different magnitude classes displayed spectra of different quality, with the lowest quality spectra obviously associated with the objects observed at the faintest magnitudes. The average S/N was considered as an initial parameter to assess the quality of the spectra:

$$\langle S/N \rangle = \frac{1}{12} \sum_{i=3}^{14} \frac{\bar{R}(\lambda_i)}{\sigma_{\bar{R}(\lambda_i)}}. \quad (6)$$

Data at the wavelengths of 374, 418, 990, and 1034 nm were omitted from the computation, as they are often affected by large random and systematic errors (see Fig. 7). On the other hand, the data point at 632 nm is included in the S/N calculation. This point can be problematic for bright objects, when in the BP-RP overlapping region the epoch reflectance values of the two spectrometers differs much more than the standard errors of the data. However, this is not a problem for the majority of SSOs, and, in particular, for those with $S/N < 50$.

The histogram of the distribution of the $\langle S/N \rangle$ value amongst the 111 818 SSOs shows a quasi-lognormal distribution (Fig. 8) with a clear peak at $\langle S/N \rangle = 13$. The same figure also shows that reflectance spectra with $\langle S/N \rangle$ values smaller than the peak value (13) are essentially due to the SSOs observed with magnitudes > 19 .

Visual inspection of randomly selected spectra with $\langle S/N \rangle > 13$ and with $\langle S/N \rangle < 13$ showed that the latter class is usually characterised by noisy spectra and the former by more accurate ones. The publication of spectra was limited to $\langle S/N \rangle > 13$ in *Gaia* DR3. The remaining spectra are waiting to be published in *Gaia* DR4 based on 66 months of *Gaia* observations (cf. the 34 months of *Gaia* DR3 observations). More transits will therefore

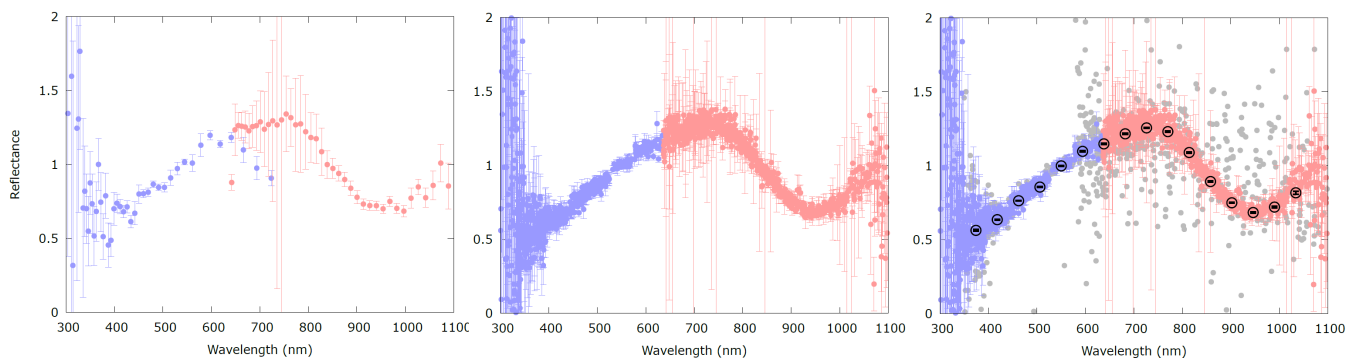


Fig. 7. Illustration of the procedure adopted to compute mean reflectance spectra. The SSO chosen as an example here is (1459) Magnya, which is a basaltic asteroid presenting a deep 950 nm-centred absorption band and a red-sloped spectrum. In the left panel, one epoch reflectance spectrum is plotted. BP and RP data are blue and red respectively. In the middle panel, all epoch reflectance spectra of Magnya are plotted. In the right panel, data filtered out by our sigma-clipping procedure are shown in grey; the over-plotted black dots correspond to the final average reflectance spectrum sampled in the 16 bands.

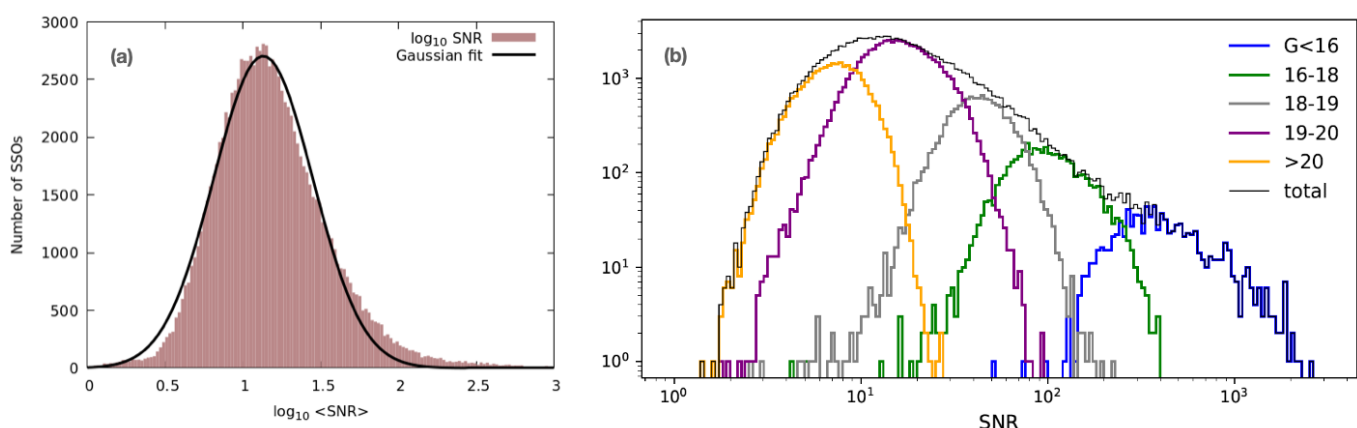


Fig. 8. (a) Mean $\langle S/N \rangle$ for the 111818 SSOs for which the pipeline produced mean reflectance spectra. (b) $\langle S/N \rangle$ for the 111 818 SSOs of different magnitude classes. Each G-band magnitude class is represented by a separate curve (from right to left): SSOs brighter than 16 mag, between 16 mag and 18 mag, between 18 mag and 19 mag, between 19 mag and 20 mag, and fainter than 20 mag. The dark grey enclosing curve is the global histogram of $\langle S/N \rangle$, the same shown in panel (a).

be averaged for *Gaia* DR4. By applying the condition $\langle S/N \rangle > 13$, a total of 60 518 SSOs was obtained.

However, the condition of having $\langle S/N \rangle > 13$ does not necessarily guarantee that the reflectance spectrum of a single asteroid will be scientifically exploitable, whereas it could still be important for population studies. Therefore, it was decided not to reject additional reflectance spectra but to flag them on a wavelength-by-wavelength basis. Namely, an array of 16 integers, one for each wavelength of the spectral bands was created with the name of `reflectance_spectrum_flag` (RSF). A value equal to 0, 1, or 2 was assigned depending on whether the data at that band were validated, suspected to be of poorer quality, or deemed to be compromised, respectively.

The procedure used to assign values to the RSF array consisted of three steps: (1) all the elements of the RSF array were initially set to zero. (2) The values of the mean reflectances and their uncertainties were explored for unreliable or non-numerical values, namely: The value of the RSF was set to 2 if the corresponding mean reflectance or its uncertainty were not numbers (NaN). The value of the RSF was set to 2 if the corresponding mean reflectance was larger than 2.5 or smaller than 0.2. This is to signal unrealistically high or low reflectance values. The value of the RSF was set to 2 if the corresponding uncertainty of the mean reflectance was larger than 0.5. (3) The values of

the mean reflectances and their uncertainties were explored in order to identify large discrepancies from an average continuous curve that would fit the discrete data. Specifically, a smoothing natural spline $S(\lambda)$ was fitted to the data points for which the corresponding RSF values were still zero after the previous step (see below for a description of how the spline was defined and implemented). The values of the RSF array were then set to 1 or 2 at those wavelengths where the mean reflectance has a distance from the smoothing spline larger than one or three times the corresponding uncertainty: if $|\bar{R}(\lambda_i) - S(\lambda_i)| > \sigma_{\bar{R}(\lambda_i)}$ then $\text{RSF}[i] = 1$; if $|\bar{R}(\lambda_i) - S(\lambda_i)| > 3 \times \sigma_{\bar{R}(\lambda_i)}$ then $\text{RSF}[i] = 2$. A value of spectral reflectance slope α_R was then calculated by fitting a straight line to those data with $\text{RSF} = 0$ and $450 \text{ nm} \leq \lambda \leq 750 \text{ nm}$ using weights equal to the inverse of the uncertainty squared. A smoothing natural spline $S'(\lambda)$ was fitted to the data points for which their corresponding RSF was still zero after the previous step and the value $z - i = 2.5 \log_{10}(S'(\lambda_z)/S'(\lambda_i))$ where $\lambda_z = 893.2 \text{ nm}$ and $\lambda_i = 748.0 \text{ nm}$ was calculated. Finally, only asteroids with $-10 \%/100 \text{ nm} < \alpha_R < 40 \%/100 \text{ nm}$ and $-0.75 < z - i < 0.5$ were validated. These latter conditions rejected only four asteroids with anomalously blue reflectance spectra, which we attributed to a flux loss of RP compared to BP.

We used the cubic spline approximation (smoothing) CSAPS² Python3 module to implement the smoothing spline with a smoothing coefficient equal to 5×10^{-7} .

4.2. Comparison against ground-based spectrophotometry and spectra

The consistency of *Gaia* DR3 SSO mean spectra against literature data was estimated by comparing spectral parameters against the same parameters from ground-based surveys and comparing spectra against literature ones. Here, we calculated spectral parameters such as the spectral slope and the equivalent of the SDSS $z-i$ colour using a well-established method (DeMeo & Carry 2013). Specifically, the spectral slope was determined from the angular coefficient of a straight line fitted to the mean reflectance values with a wavelength of between 450 and 760 nm and `reflectance_spectrum_flag = 0`. The $z-i$ colour determination was obtained by fitting a natural smoothing spline (using Python package CSAPS; smoothing coefficient = 5×10^{-7}) to all the mean reflectance values with `reflectance_spectrum_flag = 0` and then by calculating the $z-i$ colour as $z - i = 2.5 \log_{10} R_z/R_i$, where z and i represent the values of the reflectances interpolated with the spline at 748 and 893 nm, respectively.

We also downloaded literature (unsmoothed) spectra from the SMASSII website³, selected those asteroids in common with the *Gaia* DR3, and applied the same aforementioned procedure to calculate their slopes and the $z-i$ colours. We also obtained the taxonomic classification of the SMASS spectra from the SMASSII website⁴. Following known prescriptions (DeMeo et al. 2009), we grouped the classes S, Sa, Sk, Sl, Sq, and Sv into the S-complex, the classes X, Xc, Xe, Xk into the X-complex, and the classes C, Cb, Cg, Ch, Cgh into the C-complex.

Figure 9 shows that the distribution of the spectral parameters for the *Gaia* DR3 is qualitatively similar to that presented by other surveys (e.g. Parker et al. 2008; DeMeo & Carry 2013) in visible light and that SMASSII taxonomic classes and complexes overlap with the *Gaia* results as one would expect. In order to highlight more subtle differences between asteroid reflectance spectra of the *Gaia* DR3 and those of the SMASSII, we calculated the average spectral slope, the standard deviation of the spectral slope, the average $z-i$ colour, and the standard deviation of the $z-i$ colour for each complex and end-member spectral class for those asteroids that are in common between *Gaia* DR3 and the SMASSII (Fig. 10); next we compared the average values and the dispersion of the aforementioned parameters between *Gaia* and SMASSII data (Fig. 10). We found a general good agreement between *Gaia* and SMASSII spectral slopes for all taxonomic classes and complexes. On the other hand, Fig. 10 shows that *Gaia* DR3 reflectance spectra have, in general, a smaller $z-i$ colour index compared to those of SMASSII. The average difference between the $z-i$ colours of the SMASS and *Gaia* is -0.08 . This corresponds to a difference in the depth of the $\sim 1\text{-}\mu\text{m}$ band for those spectral classes with this feature. We investigate this difference in section 5.

An accurate classification of *Gaia* DR3 SSO spectral reflectances is expected for future works. However, it is possible to divide the *Gaia* DR3 SSO data set into broad taxonomic groups using slope and $z-i$ values (DeMeo & Carry 2013). To this aim, the $z-i$ versus slope plane is divided into the rectangular areas

defined in Table 3 of DeMeo & Carry (2013); we added -0.08 to the $z-i$ values of the *Gaia* DR3 in order to account for the offset found at the previous step of the analysis (as shown in Fig. 10, right panel); we classified asteroids following the same decision tree as that used by DeMeo & Carry (2013), where the slope and $z-i$ values of the SSO are compared with each region in the following order: C, B, S, L, X, D, K, Q, V, A. If an object fell in more than one class, it was designated to the last class in which it resides. If an object did not obtain a class, that is, it was outside the boundaries of the previous classes, it was designated ‘U’, which is historically used to mark unusual objects. Next, we counted the number of asteroids in each class and divided each number by the total number of *Gaia* DR3 SSOs to obtain the frequency per class, which we then displayed in Fig. 11. In the same figure, we also reported the frequency of asteroids in each class from the SDSS as classified by DeMeo & Carry (2013) – from their file `alluniq_adr4.dat`. In general, Fig. 11 shows qualitative agreement between *Gaia* DR3 and SDSS spectral classes.

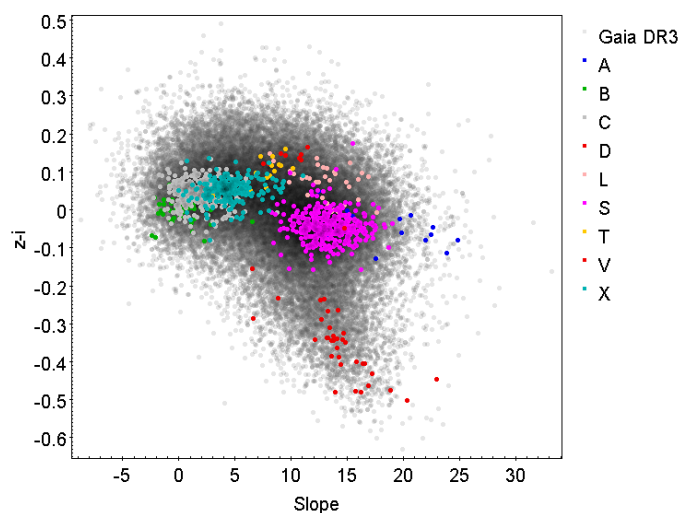


Fig. 9. $z-i$ colour vs. spectral slope of the asteroids of DR3 (grey dots). Over-plotted with circles of different colours are the same spectral parameters calculated by us (see Section 4.2) for the asteroids of SMASSII. The letters C, S, and X represent complexes, the other letters spectral classes.

Next, we calculated an RGB colour palette from the values of the slope and the $z-i$ colour, following an approach similar to that of Parker et al. (2008) (an example code is given in Appendix D). According to this palette, asteroids that are spectrally blue or spectrally neutral are given a blue colour and those that are spectrally red are given a red colour, whereas the amount of green increases with decreasing value of the $z-i$ magnitude; for example, with increasing depth of the $\sim 1\text{-}\mu\text{m}$ band. Hence, S-complex asteroids tend to have pale red to brownish colour, C-complex asteroids are blue, D- and L- types are red in colour, X-complex and K-types are magenta, and V-types are green.

Having assigned to those SSOs of the main belt their proper orbital elements from Novakovic et al. (2009), we then produced colour plots of the orbital distribution of asteroids (Fig. 12). These figures show a global gradient of colours of asteroids consistent with previous findings (Parker et al. 2008; Sergejev & Carry 2021). Asteroid collisional families are clearly distinguishable by the naked eye as groups of points with generally homogeneous colours.

The average phase angle of *Gaia*'s SSO observations is around $20 - 25^\circ$, with considerable dispersion (Fig. 3). It is

² <https://pypi.org/project/csaps/>

³ <http://smass.mit.edu>

⁴ <http://smass.mit.edu/data/smash/Bus.Taxonomy.txt>

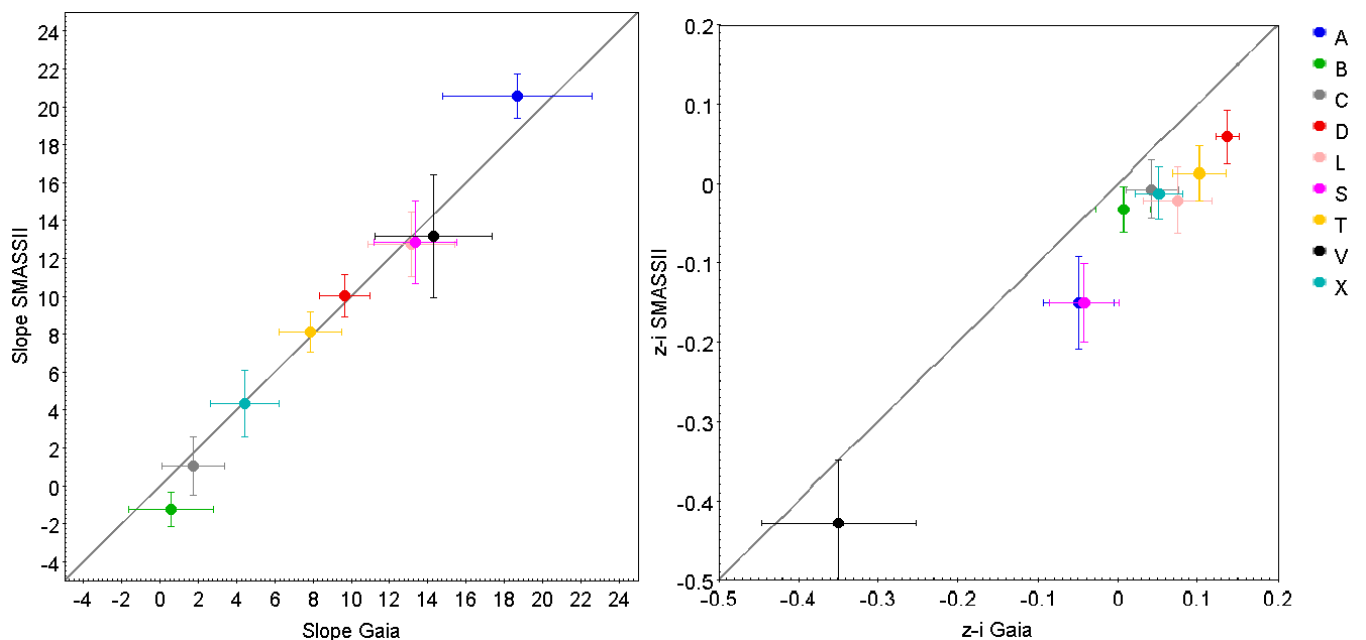


Fig. 10. Comparison of mean spectral slopes and mean $z-i$ colours of different taxonomic classes calculated on asteroids in common between *Gaia* DR3 and the SMASSII survey.

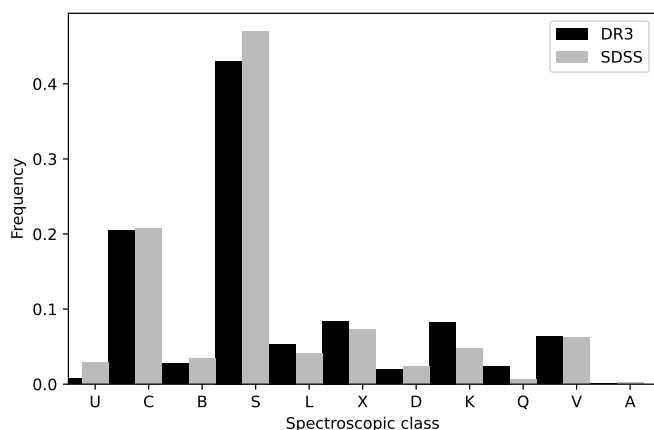


Fig. 11. Histogram of the amount of asteroids for each spectral class in the *Gaia* DR3 in comparison with the SDSS classification of DeMeo & Carry (2013).

known that phase angle has an effect on spectral reddening and the depth of the absorption bands (e.g. Taylor et al. 1971; Millis et al. 1976; Clark et al. 2002; Reddy et al. 2015; Fornasier et al. 2020). In particular, an increase of the spectral slope and decrease in the depth of the absorption bands are observed for increasing phase angle (Sanchez et al. 2012; Carvano & Davalos 2015). However, there are also physical processes that affect spectral slope and band depth, such as space weathering (Gaffey 2010; Vernazza et al. 2016; Lantz et al. 2018; Hasegawa et al. 2019) and grain size. It is therefore important to be able to disentangle the effects of such physical processes from those due to the geometry of the observations on asteroid spectra. To investigate this issue, Cellino et al. (2020) carried out spectroscopic observations of SSOs at phase angles and in the wavelength range similar to those obtained by *Gaia*. These authors selected objects in order to cover several taxonomic classes. In Appendix G, we compare *Gaia* DR3 mean reflectance spectra with those

of Cellino et al. (2020) along with other literature spectra for reference.

In general, we find satisfying agreement with literature spectra. This agreement is particularly good for asteroids with reddish, featureless spectra (e.g. D-types, such as (269) Justitia and (624) Hektor). (269) Justitia seems to be a very peculiar and interesting object based on some recent works (Cellino et al. 2020; Hasegawa et al. 2021), since this asteroid turned out to be unique and well distinct from other spectrally reddish asteroids in that sample. Good agreement between the *Gaia* reflectance spectra and those of the literature is visible for asteroids with moderate reddish spectra but mostly located in the inner main belt (e.g. for (96) Aegle we can observe that its *Gaia* reflectance spectrum goes deeper in the blue, in accordance with spectra of troilite-dominated objects; Britt et al. 1992). The *Gaia* reflectance spectra of asteroids (1904) Masevitch and (1929) Kollaa, representatives of the V-type taxonomic class in the sample of Cellino et al. (2020), show slopes that are coherent with literature ones, except for a small wavelength shift of the centre of the $1\text{-}\mu\text{m}$ absorption band. A potential caveat is that the observations of these two asteroids were made at very low phase angles for the telescope-based studies. Concerning olivine-dominated asteroids, such as the A-types, with a red spectrum and an absorption band characteristic of the olivine at $1\text{-}\mu\text{m}$, we observe marked differences between *Gaia* reflectance spectra of (246) Asporina and that of Cellino et al. (2020). However, the reflectance spectrum of Asporina of Cellino et al. (2020) is also very different from that of Bus & Binzel (2002b). *Gaia* reflectance spectra of C-type asteroids (175), (207), (261), and (3451) are in very good agreement with the ground-based ones. The absorption present in the wavelength range 400–500 nm, the ultraviolet (UV) downturn, is clearly visible. The *Gaia* spectrum of asteroid (8424) has some issues at the edge of the spectrum. Stony asteroids typical of the S-type are also included in this comparison set. These asteroids present a moderate slope between 400 and 700 nm and a tiny absorption band around $1\text{ }\mu\text{m}$, representative of the presence of silicates. We can observe that the *Gaia* reflectance spectra of asteroids (39), (82), (179), (720), (808), (1662), and (2715) are very com-

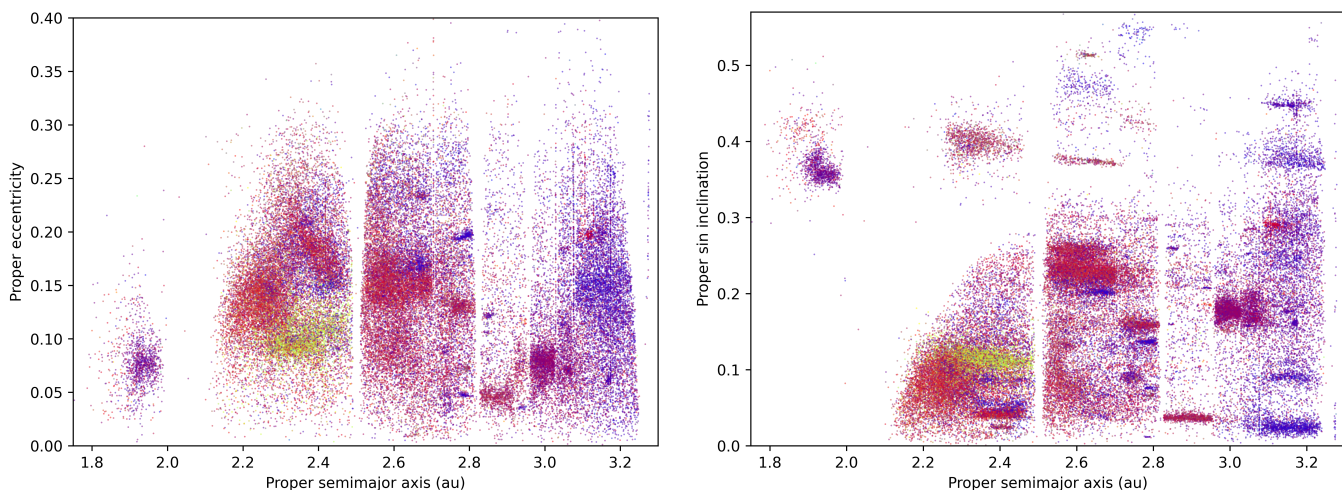


Fig. 12. Plot of the proper semi-major axis vs. proper eccentricity and sin of proper inclination for *Gaia* DR3 SSOs of the main-belt and Hungaria region. The colour of each dot is representative of the object's colour measured by *Gaia* according to the colour scheme defined in Section 4.2.

patible with S-type reflectances. With the exception of the case of asteroid (39) Laetitia, the *Gaia* reflectance spectra of all the other aforementioned SSOs have slopes similar to those of the corresponding reflectance spectra measured from ground-based telescopes. We note that for some cases, namely asteroids (720), (808), (1662), and (2715), the absorption band is weaker in *Gaia* data compared to the literature. This is as expected from the basis of results presented in Fig. 10. The *Gaia* reflectance spectrum of asteroid (43962), despite being noisy with an average S/N value of ~ 13.7 , thus very close to the rejection threshold, still shows that *Gaia* data show a nice match when superimposed on the ground-based reflectance spectra.

4.3. Comparison with literature reflectance spectra from space observations

The large majority of asteroid reflectance spectra available in the literature were obtained using ground-based telescopes. However, the reflectance spectra of some SSOs have also been obtained from space missions, and they can be compared with those derived from *Gaia* observations.

(1) Ceres is the largest asteroid and the only dwarf planet in the main belt. It is classified as C type due to its relatively flat reflectance spectrum, which presents a UV downturn typical of this spectral class (Fig. 13). The NASA space mission Dawn (Russell et al. 2004), launched in 2007, began observations of Ceres in December 2014. The Dawn framing camera (FC) instruments observed this body for at least one full rotation in three separate periods in February and April 2015 during its approach phase (at three different phase angles, distances, and image resolutions). These three epochs are referred to as rotational characterisations (RC1, RC2, and RC3). Li et al. (2016) compared spectra measured within RC1 and RC2 with several ground-based spectra and observed an increase in the spectral slope with increasing phase angle. In Fig. 13, we plot the *Gaia* mean reflectance spectrum of (1) Ceres and compare it with literature ground-based spectra (Bus & Binzel 2002b; Lazzaro et al. 2004a) and the two Dawn spectra presented in (Li et al. 2016). The agreement between *Gaia*'s reflectance spectrum and those of the literature from the ground and space is good, with the exception of a *Gaia* data point at wavelength 632 nm. The latter is very likely an artefact due to a problem in the overlapping re-

gion of the BP and the RP. It is also visible in some other spectra, in particular for very bright SSOs. The asteroid Ceres has been observed by *Gaia* at an average phase angle of 17.5° , which is approximately the same value as the previous cited ones. One can observe a slight increase in the spectral slope of Dawn's RC2 spectrum, as demonstrated by Li et al. (2016).

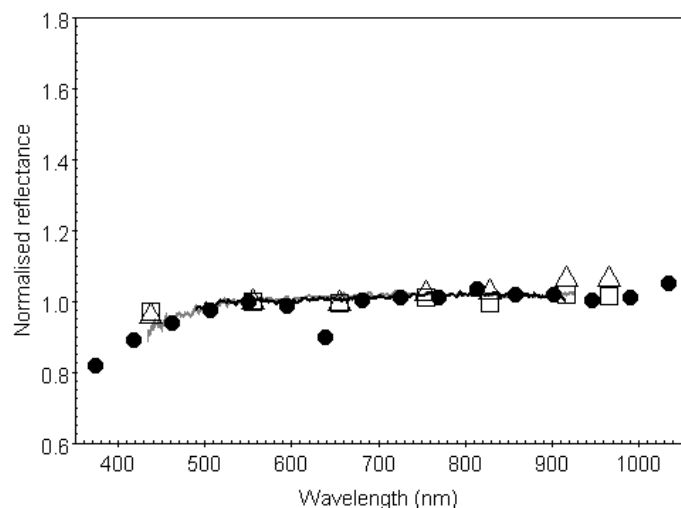


Fig. 13. *Gaia* mean reflectance spectrum of the asteroid (1) Ceres, obtained at an average phase angle of 17.5° , plotted with solid circles. Literature ground-based spectra from Bus & Binzel (2002b) and Lazzaro et al. (2004a) are shown with a grey line (phase angle of $\sim 18.6^\circ$) and a black line (phase angle of 16°), respectively. Data obtained in space by the NASA Dawn mission (Li et al. 2016) during RC1 are displayed with black open squares (phase angle between 17.2 and 17.6°), and during the RC2 with black open triangles (phase angle 42.7 to 45.3°).

(4) Vesta is the second most massive asteroid in the main belt and is spectroscopically similar to basaltic achondrite meteorites, known as Howardites, Eucrites, Diogenites (HEDs), of which it is considered to be the parent body. Vesta's reflectance spectrum presents typically two strong absorption bands around $\sim 1 \mu\text{m}$ and $\sim 2 \mu\text{m}$. The NASA Dawn mission has observed Vesta before continuing towards Ceres. Using images taken from the Dawn FC, Reddy et al. (2012) computed spectra from four different areas of Vesta, and classified these terrains as bright, corre-

sponding to bright ejecta around the 11.2-km diameter fresh impact crater Canuleia, dark, in order to highlight the dark material on the crater wall and in the surroundings of the 30-km diameter Numisia crater, grey, relative to the grey ejecta blanket of the 58-km diameter Marcia crater, and orange, which is characteristic of the 34-km diameter impact crater Oppia. These authors produced one spectrum per area, plus a global average spectrum. Reddy et al. (2012) explained that fresh impact craters have higher reflectances than background surface and deeper absorption bands. In Fig. 14, we plotted the *Gaia* reflectance spectrum against literature ground-based spectra (Bus & Binzel 2002b; Binzel et al. 2019) from the MITHNEOS survey⁵ and the five space-based Dawn spectra. The *Gaia* spectrum presents the same artefact already detected for the Ceres spectrum at $\lambda = 632$ nm. This point is affected by the overlapping of BP and RP. Otherwise, the *Gaia* spectrum is very similar to both the ground-based and the space-based spectra in its blue part. Its spectral slope is consistent with that of ground-based spectra. The *Gaia* spectrum appears less deep in the $1\text{-}\mu\text{m}$ absorption band than the ground-based ones but it is similar to the grey area spectrum. According to Reddy et al. (2012), most of Vesta's surface is covered with grey material, which could explain its match with the *Gaia* spectrum.

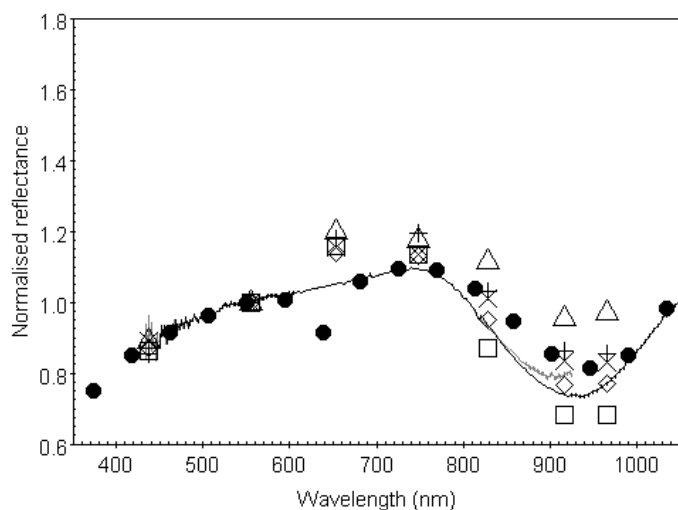


Fig. 14. *Gaia* mean reflectance spectrum of the asteroid (4) Vesta, observed at an average phase angle of 21.3° , shown with black circles. Two ground-based spectra from Bus & Binzel (2002b), observed at a phase angle of 11.9° , and from MITHNEOS survey, observed at a phase angle of 23.5° , are shown with grey and black lines, respectively. Spectra from the NASA Dawn mission (Reddy et al. 2012) for the bright, dark, grey, and orange terrains are plotted, respectively, with black open squares, black open upside down triangles, black crosses, and black plus symbols. The red spectrum, plotted with black open diamonds, corresponds to the global average spectrum of Vesta. Vesta spectra presented in (Reddy et al. 2012) were normalised at $\lambda = 750$ nm, and therefore we re-normalised them at $\lambda = 550$ nm. These spectra were obtained at a phase angle of 30° .

(21) Lutetia is an M-type asteroid (Tholen 1989). It was visited in 2010 by the ESA mission Rosetta on its way to comet 67P/Churyumov-Gerasimenko. Rosetta observed Lutetia using the Optical, Spectroscopic, and Infrared Remote Imaging System (OSIRIS), which includes a wide-angle and a narrow-angle camera (WAC and NAC, respectively; Sierks et al. 2011). In Fig. 15, we plot the *Gaia* mean reflectance spectrum together with literature ground-based spectra and the Rosetta spectra.

There is an excellent match between all spectra. The slope of the *Gaia* reflectance spectrum is also consistent with those from the literature reflectance spectra.

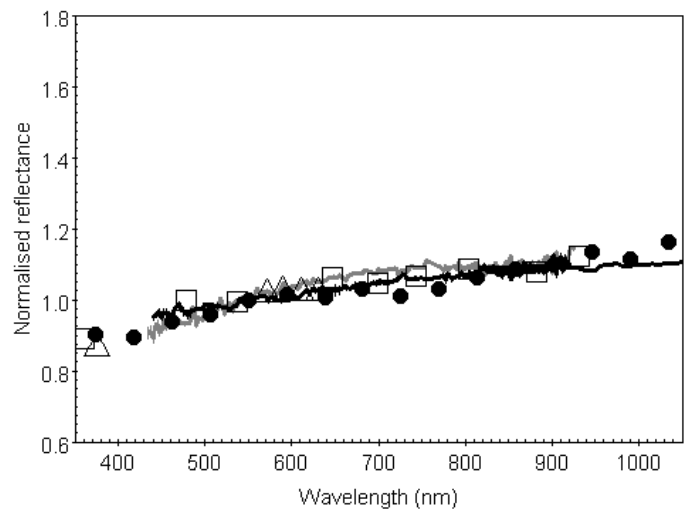


Fig. 15. *Gaia* mean reflectance spectrum of the asteroid (21) Lutetia is plotted, with black circles, together with literature ground-based spectra (grey line) and data obtained by the ESA Rosetta mission using OSIRIS NAC (black open square) and OSIRIS WAC (black open upside down triangle) at a phase angle of 7.74° (Sierks et al. 2011).

(433) Eros is a near-Earth and Mars-crossing asteroid that has been visited by the NASA Near Earth Asteroid Rendezvous (NEAR) Shoemaker spacecraft in the early 2000s (Veveřka et al. 2000). Eros is spectroscopically consistent with a silicate-based composition and classified as S-type (Bus & Binzel 2002b). Several spectra of Eros were measured by NEAR, one during the approach phase at large phase angles (between 49° and 55°) and two during the flyby phase at even larger phase angles (82° and 112°). In Fig. 16, we compare the *Gaia* reflectance spectrum with the ones obtained by the NEAR mission and two additional reflectance spectra acquired from ground-based telescopes (Vilas & McFadden 1992; Binzel et al. 2019). The slope of the *Gaia* spectrum is slightly less red than the other ones. The depth of the $1\text{-}\mu\text{m}$ absorption band is intermediate between those of the ground-based spectra, but slightly less intense than that measured by the NEAR mission.

(253) Mathilde is a main belt asteroid that the NASA Shoemaker mission flew by on its way to Eros. In Fig. 17, we plotted the *Gaia* reflectance spectrum compared to those obtained by the NEAR mission and also with spectra that were obtained from ground-based telescopes. The agreement between all spectra is quite excellent.

(951) Gaspra is an S-type asteroid belonging to the Flora family (Nesvorný et al. 2015). Gaspra was visited by the NASA Galileo spacecraft in October 1991. Figure 18 reveals a very good match between the *Gaia* mean reflectance spectrum and the ground-based one from Xu et al. (1995). Spectral slopes of all the compared spectra are also mutually consistent. The $1\text{-}\mu\text{m}$ -absorption is deeper in all the reflectance spectra obtained from the Galileo mission than in the one obtained by *Gaia*.

(2867) Šteins is a main-belt asteroid with a reflectance spectrum that is quite rare. It belongs to the E type spectral class. The ESA Rosetta mission flew by Šteins in September 2008. Several spectra were taken using the OSIRIS cameras (Keller et al. 2010). In Fig. 19, we compared the *Gaia* mean reflectance spectrum with a ground-based one from Barucci et al. (2005) and the

⁵ <http://smass.mit.edu/data/spex/sp86/>

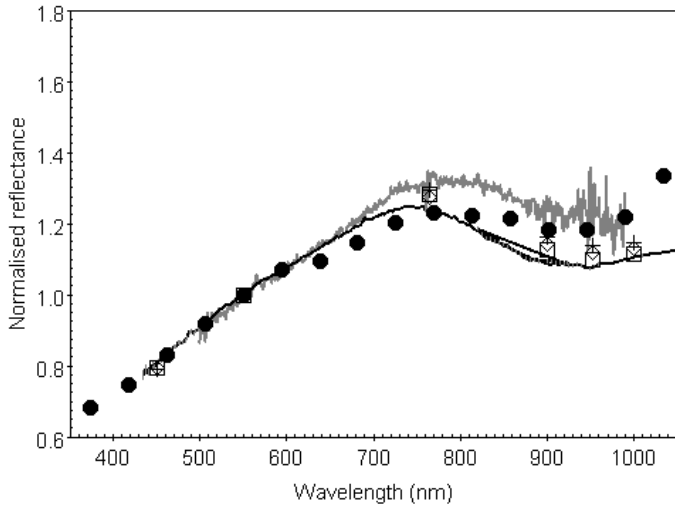


Fig. 16. *Gaia* mean reflectance spectrum of the asteroid (433) Eros, shown with black circles, together with ground-based spectra from Vilas & McFadden (1992) and Binzel et al. (2019) represented with a grey and a black line, respectively. Data obtained in space by the NASA NEAR Shoemaker mission (Veverka et al. 2000) during the approach, at a phase angle of between 49 and 55°, and during the flyby at phase angles of 82° and 112° are shown with open diamonds, open squares, and black crosses, respectively.

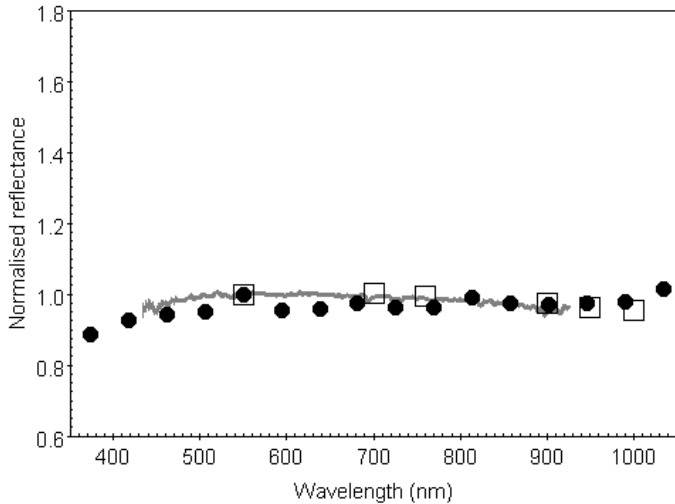


Fig. 17. *Gaia* mean reflectance spectrum of the asteroid (253) Mathilde, shown with black circles, together with ground-based spectra from Bus & Binzel (2002b) shown as a grey line, and data obtained in space by the NASA NEAR Shoemaker mission (Clark et al. 1999) with open squares (NEAR spectrum was derived from the images taken at an average solar phase angle of 41°).

ones derived from Rosetta data. We find good agreement with the *Gaia* spectrum and those presented by Barucci et al. (2005). The slope of the Rosetta mission reflectance spectra appears less steep, but the overall comparison is also remarkable when taking into account the fact that the data from the Rosetta mission were acquired from a wide range of phase angles. The upturning of the *Gaia* data beyond 1000 nm is probably due to an artefact created by the method used for the calculation of the reflectance and by the ‘alien’ photons problem (see Section 5).

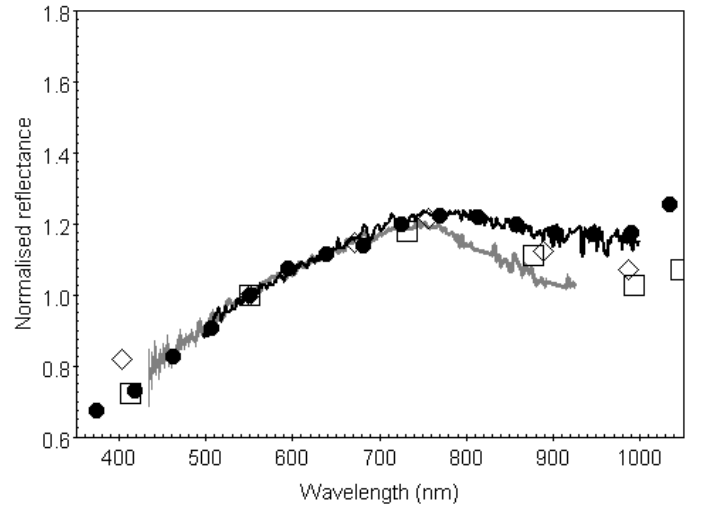


Fig. 18. *Gaia* mean reflectance spectrum of the asteroid (951) Gaspra, shown with black circles, together with literature ground-based spectra of Bus & Binzel (2002b) and Xu et al. (1995) with grey and black lines, respectively. Data obtained in space by NASA Galileo mission (Granahan et al. 1994) at phase angles of 51° and 31° are also shown with open squares and diamonds, respectively.

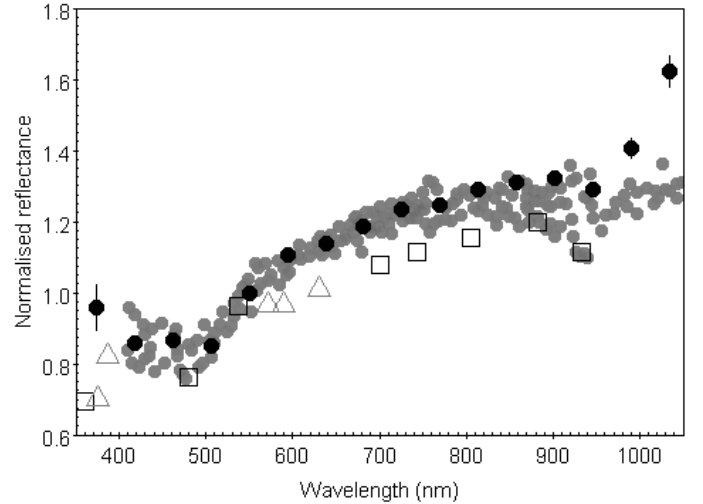


Fig. 19. *Gaia* mean reflectance spectrum of the asteroid (2867) Šteins, shown with black circles together with literature ground-based spectra from Barucci et al. (2005), with grey circles, and data obtained in space by the ESA Rosetta mission using OSIRIS NAC, black open squares, and OSIRIS WAC, black open upside-down triangle (phase angles between 0 and 132°, Keller et al. 2010).

4.4. *Gaia* view of space weathering in S-types

First of all, we selected asteroids with *Gaia* reflectance spectra compatible with spectral classes within the S-complex and belonging to collisional families (Nesvorný et al. 2015). We did this by adopting the same boundaries in the spectral slope versus $z-i$ colour space as in DeMeo & Carry (2013) for the S-complex. In particular, here, we used $6 < \text{spectral slope} < 25 \text{ \%}/100 \text{ nm}$ and $-0.005 < z-i < -0.265$. We found that there are 21 909 SSOs with *Gaia* spectral properties within this region, 9 225 of which belong to known asteroid families according to the family identification of Nesvorný et al. (2015). The age is known for several of these families, making it possible to study the variation of SSO spectral parameters as a function of age.

Table 2. S-type families for which we calculated an average spectral slope and z-i colour. Ages are from Brož et al. (2013). N_{fam} and N_{ref} are the number of family members and the number of asteroids used to calculate the average spectral slope and z-i colour.

Name	Age (Gyr)	Uncertainty (Gyr)	Phase angle (°)	N_{fam}	N_{ref}	Slope (%/100 nm)	Uncertainty (%/100 nm)	z-i	Uncertainty
Juno	0.7	0.3	20.8	1684	65	10.80	0.37	-0.074	0.009
Flora	0.9	0.3	22.7	13786	1532	12.62	0.07	-0.068	0.001
Eunomia	2.5	1.0	19.5	5670	1277	12.84	0.07	-0.054	0.001
Massalia	0.7	0.1	22.2	6424	113	10.70	0.23	-0.071	0.006
Koronis	2.5	1.0	17.5	5949	596	11.92	0.09	-0.055	0.002
Maria	3.0	1.0	19.5	2940	455	12.35	0.10	-0.054	0.002
Merxia	0.3	0.2	18.9	1215	62	11.33	0.35	-0.078	0.009
Herta	1.5	0.5	22.0	19073	927	12.58	0.10	-0.065	0.002
Agnia	0.2	0.1	18.1	2125	55	10.54	0.29	-0.086	0.008
Gefion	0.48	0.05	18.5	2547	381	12.19	0.13	-0.062	0.002
Innes	0.7	0.1	20.1	1295	115	11.00	0.22	-0.067	0.005

However, because asteroids and asteroid families of the outer main belt tend to be observed with smaller phase angles than those of the inner main belt, it is important to correct the spectral slope and the z-i colour for potential dependence with the phase angle. To this aim, we fitted a straight line to the distribution of the spectral slope as a function of the average phase angle at which S-complex SSOs were observed by *Gaia*. We only used those SSOs that have an average reflectance spectrum with a S/N of higher than 50 and with an average phase angle of between 12 and 20 degrees. We found a value of the Pearson's correlation between phase angle and spectral slope of 0.30, which suggests a weak positive correlation between these two quantities. The fit of a straight line to the data resulted in an angular slope coefficient of 0.25 ± 0.04 %/100 nm / degree (1σ). On the other hand, the z-i colour did not show a dependence with phase angle, as the Pearson correlation is -0.1; in addition, the angular coefficient of a straight line fit is only -0.04 ± 0.01 z-i mag / degree.

For each member of the S-type asteroid families from the catalogue of Nesvorný et al. (2015) that have known ages and a sufficient number (>10) of SSOs with *Gaia* DR3 mean reflectance spectra (Table 2), we calculated the spectral slope and z-i colour following the procedure described above. We then calculated the average phase angle of each family, α , the mean spectral slope, ξ , and mean z-i, and the standard errors of these means. We calculated a corrected mean spectral slopes ξ_C at a common phase angle of 20.6° by applying Eq. 7:

$$\xi_C = \xi - 0.25(\alpha - 20.6), \quad (7)$$

where 0.25 is the angular slope coefficient determined before. This correction is needed to take into account the spectral slope – phase angle dependence of S-type asteroids. On the other hand, we did not correct the z-i colours for the phase angle. Results are shown in Fig. 20. The correlation between z-i colour and the logarithm of the family age is very robust, with a Pearson correlation coefficient of 0.91 (p value = 0.0001). The correlation between the spectral slope and the logarithm of the family age has a Pearson correlation coefficient of 0.67 (p value = 0.023).

5. Discussion

Compared to ground-based observations, the *Gaia* reflectance spectra extend, in general, to bluer wavelengths. For the brightest objects, the data point at 374 nm is typically usable. This is useful to distinguish the UV drop-off of otherwise featureless spectra, such as those of asteroids belonging to the B or F class in the Tholen taxonomy (see Cellino et al. 2020). However, for

the faintest SSOs, which form the majority, the reflectance values at 374 nm (and in some cases also those at 418 nm) are affected by large errors and sometimes flagged as anomalous by our internal validation. This is due to the larger uncertainties in the calibrated BP spectra in the wavelength range [350, 400] nm, possibly extending to 450 nm at this stage in the mission (Fig. 4). A relatively small number of astronomical sources have significant flux in this wavelength range, making the calibration task more challenging.

The data points at the very red end of the spectrum, namely at wavelengths longer than ~ 950 nm, are also to be used with care, in particular for the faintest SSOs. These points can often deviate from the expected reflectance more than their statistical error bars. This is in part due to the drop-off in the sensitivity of the RP at those wavelengths.

A comparison between *Gaia* mean reflectances and those obtained from telescopes on the ground and in space for a selected sample of SSOs reveals a satisfactory match (sections 4.2 and 4.3), independently of the SSO spectral class and size. However, spectra can legitimately differ if an asteroid has spectral variability due, for example, to non-uniform composition and the comparison spectrum is not a rotational average. The publication of SSO epoch reflectance spectra in later releases will also allow asteroid spectral variability to be considered.

It is clear that XP reflectances of SSOs are in general affected by larger relative uncertainties compared to astrometry and G-band photometry for the same objects. This is due to a number of factors, such as (i) the dispersive nature of the spectroscopic data, which lowers the number of photo-electrons per pixel compared to data obtained from the astrometric field (the largest portion of the *Gaia* focal plane is covered with CCDs devoted to astrometric and unfiltered photometric measurements); (ii) the position of the BP and RP instruments at the end of the transit on the focal plane, which means that an object can move away from the window before reaching the BP and RP detectors; and (iii) the difficulty in applying the wavelength calibration for moving objects, the latter requiring a special procedure compared to Galactic stellar sources and extragalactic sources. However, the large number of SSOs for which *Gaia* produced reflectance spectra is invaluable for asteroid population studies, as showcased by this work. Given the distribution of the uncertainties in the spectral data (Fig. 8), we chose to limit the average spectral S/N to 13 for the *Gaia* DR3. More data are expected to be published with the *Gaia* DR4 and later releases.

The average difference between the z-i colours of the SMASS and *Gaia* is -0.08 (see Fig. 10). In order to understand

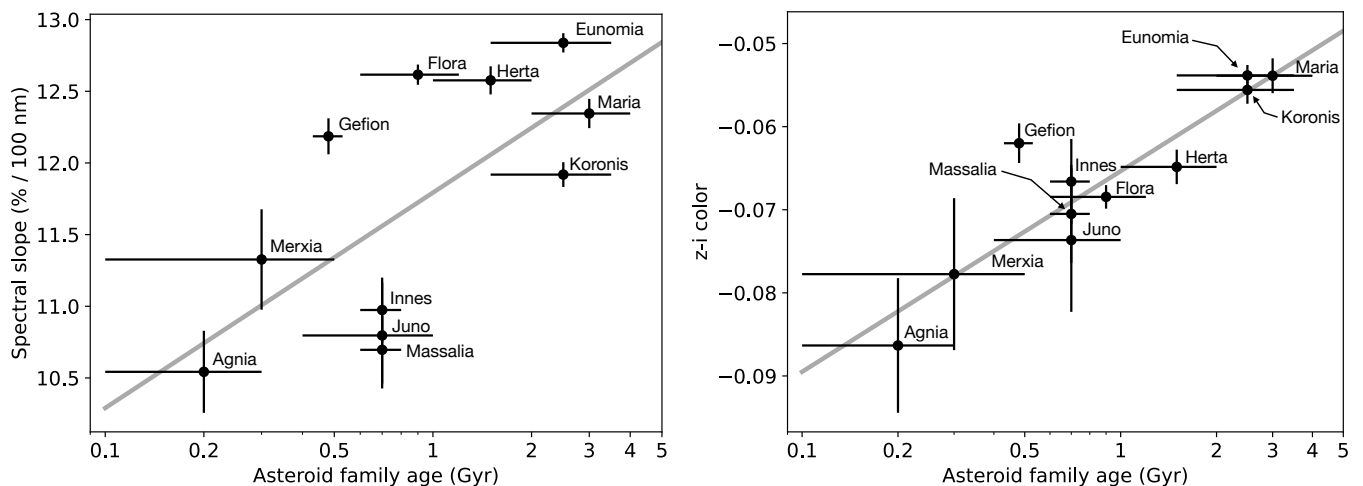


Fig. 20. Left panel: *Gaia* DR3 mean and standard deviation of the spectral slope of S-type families plotted against family age. Right panel: Mean and standard deviation of the $z-i$ colour of S-type families plotted against family age. No correction for the composition was applied to either of the plots (see Section 5).

if this difference could be due to the choice of solar analogues, we compared the solar analogue used for the production of the *Gaia* reflectances with those typically used in asteroid astronomical observations from the ground. Under the assumption that SMASS and *Gaia* observed the same asteroid spectrum, it is easy to demonstrate that

$$(z - i_{SMASS}) - (z - i_{Gaia}) = z - i \left(\frac{\text{Gaia solar analogue}}{\text{SMASS solar analogue}} \right). \quad (8)$$

We calculated the right-hand term of Eq. 8 between the mean solar analogue spectrum used for the production of the *Gaia* reflectances and each mean spectrum of the following trusted solar analogues typically used in the literature: SA93-101, Hyades64, SA98-978, SA102-1081, BS4486, SA107-684, SA107-998, SA110-361, 16CygB, SA112-1333, and SA115-271 (Marsset et al. 2020). We find that the $z-i$ of these ratios has a mean value of -0.007 and standard deviation of 0.009 . Given this evidence, it is therefore reasonable to assume that the difference in the $z-i$ values between *Gaia* and the SMASS is unlikely to be due to the choice of solar analogues. Other effects that could explain this discrepancy are described below.

Raw BP and RP spectra are affected by energy redistribution arising from broad wings of the star image profiles. As a result, each sample in the spectrum, in addition to the *local* photons, will contain *alien* photons with different wavelengths. As the wings of stellar images in the focal plane are quite large, a considerable portion of the photons from the yellow-red part of the spectrum will fall into samples covering the UV and blue wavelength ranges and vice versa. The internal calibration of the BP and RP spectra does not remove this effect and therefore the spectra used to generate the SSO reflectance spectra in *Gaia* DR3 will be affected by this contamination by *alien* photons. This implies that when an SSO spectrum is divided by the spectrum of a solar analogue, the deviation from the theoretical reflectance spectrum is a function of the difference in shape between the SSO spectrum and that of the solar analogue. In Appendix F, we suggest formulas for correcting the *Gaia* spectral parameters (slope and $z-i$ colours) using the SMASSII as a reference. The user should exercise particular caution when using those formulas, which only represent an average case, because of the large scatter in the data.

The average reflectances of SSOs with colours in the S-type range show a trend of increasing spectral slope with increasing phase angle (Fig. E.1). This is expected, and has been noted from astronomical observations (Binzel et al. 2019) and laboratory spectra of S-type analogue meteorites such as the ordinary chondrites (Sanchez et al. 2012; Brunetto et al. 2015). The value of $0.25\% / 100 \text{ nm} / \text{degree}$ that we derive here appears to be larger than those obtained by previous studies: for instance, Nathues (2010) found a value of $0.067\% / 100 \text{ nm} / \text{degree}$ with increasing phase angle in the range between 2 and 24 degrees, although this range is different from that observed by *Gaia* (Fig. E.1). On the other hand, a laboratory study of ordinary chondrites found a minimal spectral slope increase with increasing phase angle when the latter is below 30 degrees (Sanchez et al. 2012), which is the case for *Gaia* data in general. Perna et al. (2018b) also conducted a study of the spectral variation with phase angle on near-Earth asteroids. They showed that, for low-albedo and spectroscopically featureless asteroids, such as those of the C-type and D-type, no phase reddening is visible. However, these authors also identified strong phase reddening (for very large phase angles) for olivine-dominated asteroids, such as A-types and Q-types. This last result is in accordance with the study of (Sanchez et al. 2012), where it is shown that olivine-rich ordinary chondrites are those most influenced by phase reddening.

For SSOs that have spectral slope and $z-i$ colours consistent with the C-type asteroids ($-5 < \text{slope} < 6\% / 100 \text{ nm}$ and $-0.20 < z - i < 0.17$ as in DeMeo & Carry 2013), we find that the distribution of the slopes as a function of the phase angle has a Pearson coefficient of 0.03, which indicates that there is no correlation between phase angle and spectral slope. This is consistent with other studies, such as that by Lantz et al. (2018), who found no evidence of spectral reddening with increasing phase angle on B-, C-, and Ch-types.

Understanding the implications of the illumination and observation geometry, for example, the phase angle or the heliocentric distance—the latter affecting the surface temperature of the asteroids (Sanchez et al. 2012)—, is important for discriminating among the effects of asteroid ages and composition on the reflectance spectrum. The age determines the exposure of a surface to space weathering agents. It is expected that this exposure can affect the spectral parameters. Indeed, here we show that the slope of the average reflectance spectra for asteroids of

the S-complex increases with increasing age (Fig. 20). This figure also shows an important dispersion of the slope versus age in S-type families with respect to a common trend. This dispersion is probably caused by the fact that we did not correct for the composition of the asteroid. Correction for the composition has been shown to be important in particular for the very young families (Vernazza et al. 2008). Nevertheless, even without correction for composition, the trend of increasing spectral slope with age is clearly visible in the *Gaia* data. In addition, the correlations between the age and the spectral slope and the age and the z-i colour for S-type families of Fig. 20 are unlikely to be caused by composition differences between the families. This is because it has been shown that the closeness of the match between spectra of S-complex families and those of ordinary chondrite meteorites of subtypes LL, L, and H is not correlated with the spectral slopes and z-i values of the families (Vernazza et al. 2014). The correlation between the z-i colour and the asteroid family age is even tighter and more clear in the *Gaia* data. Using the collisional family ages from the work of Spoto et al. (2015) increases the scatter in the data of Fig. E.1, whereas the correlations between the spectral slope and the z-i colour with the family ages remains. Spoto et al. (2015) assumed zero initial scatter in the semi-major axis of family members, which would be due to the post-collision velocity dispersion of the fragments. Their family ages are therefore driven only by subsequent evolution due to the Yarkovsky effect. Therefore, the provided ages should be considered as upper limits.

6. Conclusions

The *Gaia* DR3 contains the largest space-based survey of reflectance spectra of Solar System small bodies observed in the visible range of the spectrum.

This article presents the procedures used to compute the mean reflectance spectrum of Solar System small bodies (SSOs) from calibrated epoch spectra and a model solar analogue spectrum. Some filtering based on the quality of the reflectance spectra was applied, leading to a catalogue of 60 518 mean reflectances sampled in 16 bands. Each mean reflectance spectrum corresponds to one SSO. Hence, the catalogue contains 60 518 different SSOs. An array of flags (one value per wavelength-band) for each spectrum is provided to indicate the quality of the measurement of the band.

In order to perform an external validation, we compared *Gaia* SSO reflectance spectra to literature spectra obtained by ground-based and space-borne telescopes. We show that this comparison reveals a good overall match. We conclude that the spectra presented in the DR3 are of good quality and show good consistency with the literature. As expected, the *Gaia* DR3 SSO spectra show a correlation between the spectral slope and the age of S-type asteroids belonging to collisional families. The *Gaia* DR3 SSO spectra also reveal a correlation between the z-i colour and the age of S-type collisional families.

The *Gaia* DR3 is a worthwhile survey that will help the community to better understand the SSO population. *Gaia* DR4 is expected to outperform the DR3 given that the former will contain a larger sample of asteroid reflectances and that these reflectances will be computed using twice as many data as were used for the DR3. The quality of the data will definitely increase and could allow us to refine the spectral bands selected for DR3. *Gaia* spectra will allow us to develop a *Gaia* spectral taxonomy that will be one of the products of the *Gaia* DR4. This will make it possible to link asteroid mass and bulk density information (expected to be one of the products of the *Gaia* DR4) with the

surface reflectance properties of asteroids. It will also allow us to derive separate relations from the magnitude–phase relations derived by *Gaia* for different classes of objects, with a possible dependence on the geometric albedo.

References

- Abe, M., Takagi, Y., Kitazato, K., et al. 2006, *Science*, 312, 1334
Ahn, C. P., Alexandroff, R., Allende Prieto, C., et al. 2012, *ApJS*, 203, 21
Albareti, F. D., Allende Prieto, C., Almeida, A., et al. 2017, *ApJS*, 233, 25
Astropy Collaboration, Price-Whelan, A., Sipőcz, B. M., et al. 2018, *AJ*, 156, 123
Barucci, M. A., Fulchignoni, M., Fornasier, S., et al. 2005, *A&A*, 430, 313
Bell, J. F., Owensby, P. D., Hawke, B. R., & Gaffey, M. J. 1988, in *Lunar and Planetary Science Conference*, Vol. 19, *Lunar and Planetary Science Conference*, 57
Belton, M. J. S., Chapman, C. R., Thomas, P. C., et al. 1995, *Nature*, 374, 785
Belton, M. J. S., Veverka, J., Thomas, P., et al. 1992, *Science*, 257, 1647
Binzel, R. P., DeMeo, F. E., Turtelboom, E. V., et al. 2019, *Icarus*, 324, 41
Boch, T. & Fernique, P. 2014, in *Astronomical Society of the Pacific Conference Series*, Vol. 485, *Astronomical Data Analysis Software and Systems XXIII*, ed. N. Manset & P. Forshay, 277
Bonnarel, F., Fernique, P., Bienaymé, O., et al. 2000, *A&AS*, 143, 33
Bottke, William F., J., Rubincam, D. P., & Burns, J. A. 2000, *Icarus*, 145, 301
Bottke, William F., J., Vokrouhlický, D., Rubincam, D. P., & Nesvorný, D. 2006, *Annual Review of Earth and Planetary Sciences*, 34, 157
Bottke, W. F., Brož, M., O'Brien, D. P., et al. 2015, in *Asteroids IV*, 701–724
Breddels, M. A. & Veljanoski, J. 2018, *A&A*, 618, A13
Britt, D. T., Bell, J. F., Haack, H., & Scott, E. R. D. 1992, *Meteoritics*, 27, 207
Brož, M., Morbidelli, A., Bottke, W. F., et al. 2013, *A&A*, 551, A117
Brunetto, R., Loeffler, M. J., Nesvorný, D., Sasaki, S., & Strazzulla, G. 2015, in *Asteroids IV* (P. Michel, et al. eds.) University of Arizona Press, Tucson., 597
Brunetto, R., Vernazza, P., Marchi, S., et al. 2006, *Icarus*, 184, 327
Burbine, T. H. & Binzel, R. P. 2002, *Icarus*, 159, 468
Bus, S. J. & Binzel, R. P. 2002a, *Icarus*, 158, 146
Bus, S. J. & Binzel, R. P. 2002b, *Icarus*, 158, 106
Bus, S. J., Vilas, F., & Barucci, M. A. 2002, *Asteroids III*, W. F. Bottke Jr., A. Cellino, P. Paolicchi, and R. P. Binzel (eds), University of Arizona Press, Tucson., 169
Carrasco, J. M., Weiler, M., Jordi, C., et al. 2021, *A&A*, 652, A86
Carry, B. 2018, *A&A*, 609, A113
Carvano, J. M. & Davalos, J. A. G. 2015, *A&A*, 580, A98
Cellino, A., Bendjoya, P., Delbo', M., et al. 2020, *A&A*, 642, A80
Chambers, K. C., Magnier, E. A., Metcalfe, N., et al. 2016, *ArXiv e-prints* [arXiv:1612.05560]
Chapman, C. R., Gaffey, M., & McFadden, L. 2005, *NASA Planetary Data System*, EAR
Clark, B. E., Bell, J. F., Fanale, F. P., & Lucey, P. G. 1993, in *Lunar and Planetary Science Conference, Lunar and Planetary Science Conference*, 299
Clark, B. E., Helfenstein, P., Bell, J. F., et al. 2002, *Icarus*, 155, 189
Clark, B. E., Veverka, J., Helfenstein, P., et al. 1999, *Icarus*, 140, 53
Davis, D. R., Chapman, C. R., Greenberg, R., Weidenschilling, S. J., & Harris, A. W. 1979, in *Asteroids*, ed. T. Gehrels & M. S. Matthews, 528–557
Davis, D. R., Chapman, C. R., Weidenschilling, S. J., & Greenberg, R. 1985, *Icarus*, 62, 30
Davis, D. R., Durda, D. D., Marzari, F., Campo Bagatin, A., & Gil-Hutton, R. 2002, in *Asteroids III*, 545–558
De Angeli et al. 2022, *A&A* in prep.
de Leon, J., Pinilla-Alonso, N., Campins, H., et al. 2018, in *AAS/Division for Planetary Sciences Meeting Abstracts*, Vol. 50, *AAS/Division for Planetary Sciences Meeting Abstracts #50*, 310.05
Delbo, M., Libourel, G., Wilkerson, J., et al. 2014, *Nature*, 508, 233
DeMeo, F. E., Alexander, C. M. O., Walsh, K. J., Chapman, C. R., & Binzel, R. P. 2015, in *Asteroids IV* (P. Michel, et al. eds.) University of Arizona Press, Tucson., 13
DeMeo, F. E., Binzel, R. P., Slivan, S. M., & Bus, S. J. 2009, *Icarus*, 202, 160
DeMeo, F. E., Burt, B. J., Marsset, M., et al. 2022, *Icarus*, 380, 114971
DeMeo, F. E. & Carry, B. 2013, *Icarus*, 226, 723
DeMeo, F. E. & Carry, B. 2014, *Nature*, 505, 629
Devogèle, M., Moskovitz, N., Thirouin, A., et al. 2019, *AJ*, 158, 196
Elkins-Tanton, L. T., Asphaug, E., Bell, J., et al. 2016, in *47th Annual Lunar and Planetary Science Conference, Lunar and Planetary Science Conference*, 1631
Erasmus, N., McNeill, A., Mommert, M., et al. 2019, *The Astrophysical Journal Supplement Series*, 242, 15
Fabricius, C., Høg, E., Makarov, V. V., et al. 2002, *A&A*, 384, 180
Farinella, P., Davis, D. R., Paolicchi, P., Cellino, A., & Zappala, V. 1992, *A&A*, 253, 604

- Farinella, P., Paolicchi, P., Tedesco, E. F., & Zappala, V. 1981, *Icarus*, 46, 114
- Flewelling, H. A., Magnier, E. A., Chambers, K. C., et al. 2020, *ApJS*, 251, 7
- Fornasier, S., Dotto, E., Hainaut, O., et al. 2007, *Icarus*, 190, 622, deep Impact Mission to Comet 9P/Tempel 1, Part 2
- Fornasier, S., Hasselmann, P. H., Deshapriya, J. D. P., et al. 2020, *A&A*, 644, A142
- Gaffey, M. J. 2010, *Icarus*, 209, 564
- Gaia Collaboration, Prusti, T., de Bruijne, J. H. J., et al. 2016, *A&A*, 595, A1
- Gilmore, G., Randich, S., Worley, C. C., et al. 2022, *A&A* in press
- Gomes, R., Levison, H. F., Tsiganis, K., & Morbidelli, A. 2005, *Nature*, 435, 466
- Gradie, J. & Tedesco, E. 1982, *Science*, 216, 1405
- Gradie, J. C., Chapman, C. R., & Tedesco, E. F. 1989, in *Asteroids II*, ed. R. P. Binzel, T. Gehrels, & M. S. Matthews, 316–335
- Granahan, J. C., Fanale, F. P., Robinson, M. S., et al. 1994, in *Lunar and Planetary Science Conference, Lunar and Planetary Science Conference*, 453
- Granvik, M., Morbidelli, A., Jedicke, R., et al. 2018, *Icarus*, 312, 181
- Granvik, M., Morbidelli, A., Vokrouhlický, D., et al. 2017, *Astronomy and Astrophysics*, 598, A52
- Hasegawa, S., Hiroi, T., Ohtsuka, K., et al. 2019, *PASJ*, 71, 103
- Hasegawa, S., Marsset, M., DeMeo, F. E., et al. 2021, *ApJ*, 916, L6
- Henden, A. A., Templeton, M., Terrell, D., et al. 2016, *VizieR Online Data Catalogue*, 2336
- Høg, E., Fabricius, C., Makarov, V. V., et al. 2000, *A&A*, 355, L27
- Huang, J., Ji, J., Ye, P., et al. 2013, *Scientific Reports*, 3, 3411
- Huber, D., Bryson, S. T., Haas, M. R., et al. 2016, *ApJS*, 224, 2
- Hunter, J. D. 2007, *Computing In Science & Engineering*, 9, 90
- Ivezić, Ž., Kahn, S. M., Tyson, J. A., et al. 2019, *The Astrophysical Journal*, 873, 111
- Ivezić, Ž., Kahn, S. M., Tyson, J. A., et al. 2019, *ApJ*, 873, 111
- Jordi, C., Gebran, M., Carrasco, J. M., et al. 2010, *A&A*, 523, A48
- Keller, H. U., Barbieri, C., Koschny, D., et al. 2010, *Science*, 327, 190
- Lantz, C., Binzel, R. P., & DeMeo, F. E. 2018, *Icarus*, 302, 10
- Lasker, B. M., Lattanzi, M. G., McLean, B. J., et al. 2008, *AJ*, 136, 735
- Lauretta, D. S., DellaGiustina, D. N., Bennett, C. A., et al. 2019, *Nature*, 568, 55
- Lazzaro, D., Angeli, C., Carvano, J., et al. 2004a, *Icarus*, 172, 179, special Issue: Cassini-Huygens at Jupiter
- Lazzaro, D., Angeli, C. A., Carvano, J. M., et al. 2004b, *Icarus*, 172, 179
- Li, J.-Y., Reddy, V., Nathues, A., et al. 2016, *ApJ*, 817, L22
- Libourel, G., Michel, P., Delbo, M., et al. 2017, *Icarus*, 282, 375
- Lindgren, L., Lammers, U., Hobbs, D., et al. 2012, *A&A*, 538, A78
- LSST Science Collaboration, Abell, P. A., Allison, J., et al. 2009, *arXiv e-prints*, arXiv:0912.0201
- Lucas, M. P., Emery, J. P., MacLennan, E. M., et al. 2019, *Icarus*, 322, 227
- Luo, A. L., Zhao, Y.-H., Zhao, G., et al. 2015, *Research in Astronomy and Astrophysics*, 15, 1095
- Magnier, E. A., Chambers, K. C., Flewelling, H. A., et al. 2020a, *ApJS*, 251, 3
- Magnier, E. A., Schlafly, E. F., Finkbeiner, D. P., et al. 2020b, *ApJS*, 251, 6
- Magnier, E. A., Sweeney, W. E., Chambers, K. C., et al. 2020c, *ApJS*, 251, 5
- Mainzer, A., Grav, T., Bauer, J., et al. 2011, *The Astrophysical Journal*, 743, 156
- Mainzer, A., Usui, F., & Trilling, D. E. 2015, in *Asteroids IV* (P. Michel, et al. eds.) University of Arizona Press, Tucson., 89
- Marsset, M., DeMeo, F. E., Binzel, R. P., et al. 2020, *ApJS*, 247, 73
- Marsset, M., DeMeo, F. E., Burt, B., et al. 2022, *AJ*, 163, 165
- Michel, P. 2013, *Acta Astronautica*, 90, 6
- Michel, P., Kueppers, M., Fitzsimmons, A., et al. 2021, in *European Planetary Science Congress, EPSC2021–71*
- Millis, R. L., Bowell, E., & Thompson, D. T. 1976, *Icarus*, 28, 53
- Minton, D. A. & Malhotra, R. 2009, *Nature*, 457, 1109
- Molaro, J. L., Byrne, S., & Le, J. L. 2017, *Icarus*, 294, 247
- Molaro, J. L., Walsh, K. J., Jawin, E. R., et al. 2020, *Nature Communications*, 11, 2913
- Morate, D., Marcio Carvano, J., Alvarez-Candal, A., et al. 2021, *A&A*, 655, A47
- Morbidelli, A., Bottke, W. F., Nesvorný, D., & Levison, H. F. 2009, *Icarus*, 204, 558
- Morbidelli, A., Delbo, M., Granvik, M., et al. 2020, *Icarus*, 340, 113631
- Morbidelli, A. & Raymond, S. N. 2016, *Journal of Geophysical Research: Planets*, 121, 1962
- Morbidelli, A. & Vokrouhlický, D. 2003, *Icarus*, 163, 120
- Nathues, A. 2010, *Icarus*, 208, 252
- Nesvorný, D. 2018, *ARA&A*, 56, 137
- Nesvorný, D., Brož, M., & Carruba, V. 2015, in *Asteroids IV* (P. Michel, et al. eds.) University of Arizona Press, Tucson., 297
- Nesvorný, D. & Morbidelli, A. 2012, *The Astronomical Journal*, 144, 117
- Novakovic, B., Balaz, A., Knezevic, Z., & Potocnik, M. 2009, *Serbian Astronomical Journal*, 179, 75
- Ochsenbein, F., Bauer, P., & Marcout, J. 2000, *A&AS*, 143, 23
- Olkin, C. B., Levison, H. F., Vincent, M., et al. 2021, *The Planetary Science Journal*, 2, 172
- Onken, C. A., Wolf, C., Bessell, M. S., et al. 2019, *PASA*, 36, e033
- Parker, A., Ivezić, Ž., Jurić, M., et al. 2008, *Icarus*, 198, 138
- Pérez, F. & Granger, B. E. 2007, *Computing in Science and Engineering*, 9, 21
- Perna, D., Barucci, M. A., Fulchignoni, M., et al. 2018a, *Planet. Space Sci.*, 157, 82
- Perna, D., Barucci, M. A., Fulchignoni, M., et al. 2018b, *Planet. Space Sci.*, 157, 82
- Pierens, A., Raymond, S. N., Nesvorný, D., & Morbidelli, A. 2014, *ApJ*, 795, L11
- Popescu, M., Licandro, J., Morate, D., et al. 2016, *Astronomy and Astrophysics*, 591, A115
- Popescu, M., Birlan, M., Nedelcu, D. A., Vaubaillon, J., & Cristescu, C. P. 2014, *A&A*, 572, A106
- Popescu, M., Vaduvescu, O., de León, J., et al. 2019, *A&A*, 627, A124
- R Core Team. 2013, *R: A Language and Environment for Statistical Computing*, R Foundation for Statistical Computing, Vienna, Austria
- Randich, S., Gilmore, G., Magrini, L., et al. 2022, *A&A* in press
- Raymond, S. N. & Izidoro, A. 2017, *Science Advances*, 3, e1701138
- Raymond, S. N., Izidoro, A., & Morbidelli, A. 2020, in *Planetary Astrobiology*, ed. V. S. Meadows, G. N. Arney, B. E. Schmidt, & D. J. Des Marais, 287
- Raymond, S. N. & Nesvorný, D. 2020, *arXiv e-prints*, arXiv:2012.07932
- Reddy, V., Dunn, T. L., Thomas, C. A., Moskovitz, N. A., & Burbine, T. H. 2015, in *Asteroids IV*, 43–63
- Reddy, V., Nathues, A., Le Corre, L., et al. 2012, *Science*, 336, 700
- Rivkin, A. S., Chabot, N. L., Stickle, A. M., et al. 2021, *The Planetary Science Journal*, 2, 173
- Roeser, S., Demleitner, M., & Schilbach, E. 2010, *AJ*, 139, 2440
- Rubincam, D. P. 2000, *Icarus*, 148, 2
- Russell, C. T., Coradini, A., Christensen, U., et al. 2004, *Planet. Space Sci.*, 52, 465
- Sanchez, J. A., Reddy, V., Nathues, A., et al. 2012, *Icarus*, 220, 36
- Sergeyev, A. V. & Carry, B. 2021, *A&A*, 652, A59
- Sergeyev, A. V., Carry, B., Onken, C. A., et al. 2022, *A&A*, 658, A109
- Sierks, H., Lamy, P., Barbieri, C., et al. 2011, *Science*, 334, 487
- Skrutskie, M. F., Cutri, R. M., Stiening, R., et al. 2006, *AJ*, 131, 1163
- Soubiran, C. & Triaud, A. 2004, *A&A*, 418, 1089
- Spoto, F., Milani, A., & Knežević, Z. 2015, *Icarus*, 257, 275
- Steinmetz, M., Guiglion, G., McMillan, P. J., et al. 2020a, *AJ*, 160, 83
- Steinmetz, M., Matijević, G., Enke, H., et al. 2020b, *AJ*, 160, 82
- Sugita, S., Honda, R., Morota, T., et al. 2019, *Science*, 364, 252
- Tanga, P. & Mignard, F. 2012, *Planet. Space Sci.*, 73, 5
- Tanga, P. e. a. 2022, *A&A* in prep.
- Taylor, M. B. 2005a, in *Astronomical Society of the Pacific Conference Series*, Vol. 347, *Astronomical Data Analysis Software and Systems XIV*, ed. P. Shopbell, M. Britton, & R. Ebert, 29
- Taylor, M. B. 2005b, in *Astronomical Society of the Pacific Conference Series*, Vol. 347, *Astronomical Data Analysis Software and Systems XIV*, ed. P. Shopbell, M. Britton, & R. Ebert, 29
- Taylor, M. B. 2006, in *Astronomical Society of the Pacific Conference Series*, Vol. 351, *Astronomical Data Analysis Software and Systems XV*, ed. C. Gabriel, C. Arviset, D. Ponz, & S. Enrique, 666
- Taylor, R. C., Gehrels, T., & Silvester, A. B. 1971, *AJ*, 76, 141
- Tholen, D. J. 1989, in *Asteroids II*, ed. R. P. Binzel, T. Gehrels, & M. S. Matthews, 1139–1150
- Tsiganis, K., Gomes, R., Morbidelli, A., & Levison, H. F. 2005, *Nature*, 435, 459
- van Leeuwen, F. 2007, *A&A*, 474, 653
- Vera C. Rubin Observatory LSST Solar System Science Collaboration, Jones, R. L., Bannister, M. T., et al. 2020, *arXiv e-prints*, arXiv:2009.07653
- Vernazza, P., Binzel, R. P., Thomas, C. A., et al. 2008, *Nature*, 454, 858
- Vernazza, P., Marsset, M., Beck, P., et al. 2016, *AJ*, 152, 54
- Vernazza, P., Zanda, B., Binzel, R. P., et al. 2014, *ApJ*, 791, 120
- Veveřka, J., Helfenstein, P., Lee, P., et al. 1996, *Icarus*, 120, 66
- Veveřka, J., Robinson, M., Thomas, P., et al. 2000, *Science*, 289, 2088
- Vilas, F., Larson, S. M., Hatch, E. C., & Jarvis, K. S. 1993, *Icarus*, 105, 67
- Vilas, F. & McFadden, L. A. 1992, *Icarus*, 100, 85
- Vokrouhlický, D. & Farinella, P. 2000, *Nature*, 407, 606
- Walsh, K. J., Morbidelli, A., Raymond, S. N., O’Brien, D. P., & Mandell, A. M. 2011, *Nature*, 475, 206
- Walsh, K. J., Morbidelli, A., Raymond, S. N., O’Brien, D. P., & Mandell, A. M. 2012, *Meteoritics & Planetary Science*, 47, 1941
- Waters, C. Z., Magnier, E. A., Price, P. A., et al. 2020, *ApJS*, 251, 4
- Wenger, M., Ochsenbein, F., Egret, D., et al. 2000, *A&AS*, 143, 9
- Winn, J. N. & Fabrycky, D. C. 2015, *ARA&A*, 53, 409
- Xu, S., Binzel, R. P., Burbine, T. H., & Bus, S. J. 1995, *Icarus*, 115, 1
- Zacharias, N., Finch, C., Subasavage, J., et al. 2015, *AJ*, 150, 101
- Zacharias, N., Finch, C. T., Girard, T. M., et al. 2013, *AJ*, 145, 44
- Zellner, B., Tholen, D. J., & Tedesco, E. F. 1985, *Icarus*, 61, 355
- Zolensky, M., Bland, P., Brown, P., & Halliday, I. 2006, in *Meteorites and the Early Solar System II*, ed. D. S. Lauretta & H. Y. McSween, 869

- 1 Université Côte d'Azur, Observatoire de la Côte d'Azur, CNRS, Laboratoire Lagrange, Bd de l'Observatoire, CS 34229, 06304 Nice Cedex 4, France
- 2 Institute of Astronomy, University of Cambridge, Madingley Road, Cambridge CB3 0HA, United Kingdom
- 3 Royal Observatory of Belgium, Ringlaan 3, 1180 Brussels, Belgium
- 4 INAF - Osservatorio Astrofisico di Torino, via Osservatorio 20, 10025 Pino Torinese (TO), Italy
- 5 Leiden Observatory, Leiden University, Niels Bohrweg 2, 2333 CA Leiden, The Netherlands
- 6 Department of Physics, University of Helsinki, P.O. Box 64, 00014 Helsinki, Finland
- 7 Finnish Geospatial Research Institute FGI, Geodeetinrinne 2, 02430 Masala, Finland
- 8 Astronomisches Rechen-Institut, Zentrum für Astronomie der Universität Heidelberg, Mönchhofstr. 12-14, 69120 Heidelberg, Germany
- 9 INAF - Osservatorio astronomico di Padova, Vicolo Osservatorio 5, 35122 Padova, Italy
- 10 European Space Agency (ESA), European Space Research and Technology Centre (ESTEC), Keplerlaan 1, 2201AZ, Noordwijk, The Netherlands
- 11 GEPI, Observatoire de Paris, Université PSL, CNRS, 5 Place Jules Janssen, 92190 Meudon, France
- 12 Univ. Grenoble Alpes, CNRS, IPAG, 38000 Grenoble, France
- 13 Laboratoire d'astrophysique de Bordeaux, Univ. Bordeaux, CNRS, B18N, allée Geoffroy Saint-Hilaire, 33615 Pessac, France
- 14 Department of Astronomy, University of Geneva, Chemin Pegasi 51, 1290 Versoix, Switzerland
- 15 European Space Agency (ESA), European Space Astronomy Centre (ESAC), Camino bajo del Castillo, s/n, Urbanizacion Villafranca del Castillo, Villanueva de la Cañada, 28692 Madrid, Spain
- 16 Aurora Technology for European Space Agency (ESA), Camino bajo del Castillo, s/n, Urbanizacion Villafranca del Castillo, Villanueva de la Cañada, 28692 Madrid, Spain
- 17 Institut de Ciències del Cosmos (ICCUB), Universitat de Barcelona (IEEC-UB), Martí i Franquès 1, 08028 Barcelona, Spain
- 18 Lohrmann Observatory, Technische Universität Dresden, Mommsenstraße 13, 01062 Dresden, Germany
- 19 Lund Observatory, Department of Astronomy and Theoretical Physics, Lund University, Box 43, 22100 Lund, Sweden
- 20 CNES Centre Spatial de Toulouse, 18 avenue Edouard Belin, 31401 Toulouse Cedex 9, France
- 21 Institut d'Astronomie et d'Astrophysique, Université Libre de Bruxelles CP 226, Boulevard du Triomphe, 1050 Brussels, Belgium
- 22 F.R.S.-FNRS, Rue d'Egmont 5, 1000 Brussels, Belgium
- 23 INAF - Osservatorio Astrofisico di Arcetri, Largo Enrico Fermi 5, 50125 Firenze, Italy
- 24 Max Planck Institute for Astronomy, Königstuhl 17, 69117 Heidelberg, Germany
- 25 European Space Agency (ESA, retired)
- 26 University of Turin, Department of Physics, Via Pietro Giuria 1, 10125 Torino, Italy
- 27 INAF - Osservatorio di Astrofisica e Scienza dello Spazio di Bologna, via Piero Gobetti 93/3, 40129 Bologna, Italy
- 28 DAPCOM for Institut de Ciències del Cosmos (ICCUB), Universitat de Barcelona (IEEC-UB), Martí i Franquès 1, 08028 Barcelona, Spain
- 29 Observational Astrophysics, Division of Astronomy and Space Physics, Department of Physics and Astronomy, Uppsala University, Box 516, 751 20 Uppsala, Sweden
- 30 ALTEC S.p.a, Corso Marche, 79, 10146 Torino, Italy
- 31 Särl, Geneva, Switzerland
- 32 Department of Astronomy, University of Geneva, Chemin d'Ecogia 16, 1290 Versoix, Switzerland
- 33 Mullard Space Science Laboratory, University College London, Holmbury St Mary, Dorking, Surrey RH5 6NT, United Kingdom
- 34 Gaia DPAC Project Office, ESAC, Camino bajo del Castillo, s/n, Urbanizacion Villafranca del Castillo, Villanueva de la Cañada, 28692 Madrid, Spain
- 35 Telespazio UK S.L. for European Space Agency (ESA), Camino bajo del Castillo, s/n, Urbanizacion Villafranca del Castillo, Villanueva de la Cañada, 28692 Madrid, Spain
- 36 SYRTE, Observatoire de Paris, Université PSL, CNRS, Sorbonne Université, LNE, 61 avenue de l'Observatoire 75014 Paris, France
- 37 National Observatory of Athens, I. Metaxa and Vas. Pavlou, Palaia Penteli, 15236 Athens, Greece
- 38 IMCCE, Observatoire de Paris, Université PSL, CNRS, Sorbonne Université, Univ. Lille, 77 av. Denfert-Rochereau, 75014 Paris, France
- 39 Serco Gestión de Negocios for European Space Agency (ESA), Camino bajo del Castillo, s/n, Urbanizacion Villafranca del Castillo, Villanueva de la Cañada, 28692 Madrid, Spain
- 40 Institut d'Astrophysique et de Géophysique, Université de Liège, 19c, Allée du 6 Août, B-4000 Liège, Belgium
- 41 CRAAG - Centre de Recherche en Astronomie, Astrophysique et Géophysique, Route de l'Observatoire Bp 63 Bouzareah 16340 Algiers, Algeria
- 42 Institute for Astronomy, University of Edinburgh, Royal Observatory, Blackford Hill, Edinburgh EH9 3HJ, United Kingdom
- 43 RHEA for European Space Agency (ESA), Camino bajo del Castillo, s/n, Urbanizacion Villafranca del Castillo, Villanueva de la Cañada, 28692 Madrid, Spain
- 44 ATG Europe for European Space Agency (ESA), Camino bajo del Castillo, s/n, Urbanizacion Villafranca del Castillo, Villanueva de la Cañada, 28692 Madrid, Spain
- 45 CIGUS CITIC - Department of Computer Science and Information Technologies, University of A Coruña, Campus de Elviña s/n, A Coruña, 15071, Spain
- 46 Université de Strasbourg, CNRS, Observatoire astronomique de Strasbourg, UMR 7550, 11 rue de l'Université, 67000 Strasbourg, France
- 47 Kavli Institute for Cosmology Cambridge, Institute of Astronomy, Madingley Road, Cambridge, CB3 0HA
- 48 Leibniz Institute for Astrophysics Potsdam (AIP), An der Sternwarte 16, 14482 Potsdam, Germany
- 49 CENTRA, Faculdade de Ciências, Universidade de Lisboa, Edif. C8, Campo Grande, 1749-016 Lisboa, Portugal
- 50 Department of Informatics, Donald Bren School of Information and Computer Sciences, University of California, Irvine, 5226 Donald Bren Hall, 92697-3440 CA Irvine, United States
- 51 INAF - Osservatorio Astrofisico di Catania, via S. Sofia 78, 95123 Catania, Italy
- 52 Dipartimento di Fisica e Astronomia "Ettore Majorana", Università di Catania, Via S. Sofia 64, 95123 Catania, Italy
- 53 INAF - Osservatorio Astronomico di Roma, Via Frascati 33, 00078 Monte Porzio Catone (Roma), Italy
- 54 Space Science Data Center - ASI, Via del Politecnico SNC, 00133 Roma, Italy
- 55 Institut UTINAM CNRS UMR6213, Université Bourgogne Franche-Comté, OSU THETA Franche-Comté Bourgogne, Observatoire de Besançon, BP1615, 25010 Besançon Cedex, France
- 56 HE Space Operations BV for European Space Agency (ESA), Keplerlaan 1, 2201AZ, Noordwijk, The Netherlands
- 57 Dpto. de Inteligencia Artificial, UNED, c/ Juan del Rosal 16, 28040 Madrid, Spain
- 58 Konkoly Observatory, Research Centre for Astronomy and Earth Sciences, Eötvös Loránd Research Network (ELKH), MTA Centre of Excellence, Konkoly Thege Miklós út 15-17, 1121 Budapest, Hungary
- 59 ELTE Eötvös Loránd University, Institute of Physics, 1117, Pázmány Péter sétány 1A, Budapest, Hungary
- 60 Instituut voor Sterrenkunde, KU Leuven, Celestijnenlaan 200D, 3001 Leuven, Belgium
- 61 Department of Astrophysics/IMAPP, Radboud University, P.O.Box 9010, 6500 GL Nijmegen, The Netherlands

- ⁶² University of Vienna, Department of Astrophysics, Türkenschanzstraße 17, A1180 Vienna, Austria
- ⁶³ Institute of Physics, Laboratory of Astrophysics, Ecole Polytechnique Fédérale de Lausanne (EPFL), Observatoire de Sauverny, 1290 Versoix, Switzerland
- ⁶⁴ Kapteyn Astronomical Institute, University of Groningen, Landleven 12, 9747 AD Groningen, The Netherlands
- ⁶⁵ School of Physics and Astronomy / Space Park Leicester, University of Leicester, University Road, Leicester LE1 7RH, United Kingdom
- ⁶⁶ Thales Services for CNES Centre Spatial de Toulouse, 18 avenue Edouard Belin, 31401 Toulouse Cedex 9, France
- ⁶⁷ Depto. Estadística e Investigación Operativa. Universidad de Cádiz, Avda. República Saharaui s/n, 11510 Puerto Real, Cádiz, Spain
- ⁶⁸ Center for Research and Exploration in Space Science and Technology, University of Maryland Baltimore County, 1000 Hilltop Circle, Baltimore MD, USA
- ⁶⁹ GSFC - Goddard Space Flight Center, Code 698, 8800 Greenbelt Rd, 20771 MD Greenbelt, United States
- ⁷⁰ EURIX S.r.l., Corso Vittorio Emanuele II 61, 10128, Torino, Italy
- ⁷¹ Porter School of the Environment and Earth Sciences, Tel Aviv University, Tel Aviv 6997801, Israel
- ⁷² Harvard-Smithsonian Center for Astrophysics, 60 Garden St., MS 15, Cambridge, MA 02138, USA
- ⁷³ HE Space Operations BV for European Space Agency (ESA), Camino bajo del Castillo, s/n, Urbanizacion Villafranca del Castillo, Villanueva de la Cañada, 28692 Madrid, Spain
- ⁷⁴ Instituto de Astrofísica e Ciências do Espaço, Universidade do Porto, CAUP, Rua das Estrelas, PT4150-762 Porto, Portugal
- ⁷⁵ LFCA/DAS, Universidad de Chile, CNRS, Casilla 36-D, Santiago, Chile
- ⁷⁶ SISSA - Scuola Internazionale Superiore di Studi Avanzati, via Bonomea 265, 34136 Trieste, Italy
- ⁷⁷ Telespazio for CNES Centre Spatial de Toulouse, 18 avenue Edouard Belin, 31401 Toulouse Cedex 9, France
- ⁷⁸ University of Turin, Department of Computer Sciences, Corso Svizzera 185, 10149 Torino, Italy
- ⁷⁹ Dpto. de Matemática Aplicada y Ciencias de la Computación, Univ. de Cantabria, ETS Ingenieros de Caminos, Canales y Puertos, Avda. de los Castros s/n, 39005 Santander, Spain
- ⁸⁰ Centro de Astronomía - CITEVA, Universidad de Antofagasta, Avenida Angamos 601, Antofagasta 1270300, Chile
- ⁸¹ DLR Gesellschaft für Raumfahrtanwendungen (GfR) mbH Münchener Straße 20, 82234 Weßling
- ⁸² Centre for Astrophysics Research, University of Hertfordshire, College Lane, AL10 9AB, Hatfield, United Kingdom
- ⁸³ University of Turin, Mathematical Department "G. Peano", Via Carlo Alberto 10, 10123 Torino, Italy
- ⁸⁴ INAF - Osservatorio Astronomico d'Abruzzo, Via Mentore Maggini, 64100 Teramo, Italy
- ⁸⁵ Instituto de Astronomia, Geofísica e Ciências Atmosféricas, Universidade de São Paulo, Rua do Matão, 1226, Cidade Universitária, 05508-900 São Paulo, SP, Brazil
- ⁸⁶ APAVE SUDEUROPE SAS for CNES Centre Spatial de Toulouse, 18 avenue Edouard Belin, 31401 Toulouse Cedex 9, France
- ⁸⁷ Mésocentre de calcul de Franche-Comté, Université de Franche-Comté, 16 route de Gray, 25030 Besançon Cedex, France
- ⁸⁸ ATOS for CNES Centre Spatial de Toulouse, 18 avenue Edouard Belin, 31401 Toulouse Cedex 9, France
- ⁸⁹ School of Physics and Astronomy, Tel Aviv University, Tel Aviv 6997801, Israel
- ⁹⁰ Astrophysics Research Centre, School of Mathematics and Physics, Queen's University Belfast, Belfast BT7 1NN, UK
- ⁹¹ Centre de Données Astronomique de Strasbourg, Strasbourg, France
- ⁹² Institute for Computational Cosmology, Department of Physics, Durham University, Durham DH1 3LE, UK
- ⁹³ European Southern Observatory, Karl-Schwarzschild-Str. 2, 85748 Garching, Germany
- ⁹⁴ Max-Planck-Institut für Astrophysik, Karl-Schwarzschild-Straße 1, 85748 Garching, Germany
- ⁹⁵ Data Science and Big Data Lab, Pablo de Olavide University, 41013, Seville, Spain
- ⁹⁶ Barcelona Supercomputing Center (BSC), Plaça Eusebi Güell 1-3, 08034-Barcelona, Spain
- ⁹⁷ ETSE Telecomunicación, Universidade de Vigo, Campus Lagoas-Marcosende, 36310 Vigo, Galicia, Spain
- ⁹⁸ Asteroid Engineering Laboratory, Space Systems, Luleå University of Technology, Box 848, S-981 28 Kiruna, Sweden
- ⁹⁹ Vera C Rubin Observatory, 950 N. Cherry Avenue, Tucson, AZ 85719, USA
- ¹⁰⁰ Department of Astrophysics, Astronomy and Mechanics, National and Kapodistrian University of Athens, Panepistimiopolis, Zografos, 15783 Athens, Greece
- ¹⁰¹ TRUMPF Photonic Components GmbH, Lise-Meitner-Straße 13, 89081 Ulm, Germany
- ¹⁰² IAC - Instituto de Astrofísica de Canarias, Via Láctea s/n, 38200 La Laguna S.C., Tenerife, Spain
- ¹⁰³ Department of Astrophysics, University of La Laguna, Via Láctea s/n, 38200 La Laguna S.C., Tenerife, Spain
- ¹⁰⁴ Faculty of Aerospace Engineering, Delft University of Technology, Kluyverweg 1, 2629 HS Delft, The Netherlands
- ¹⁰⁵ Radagast Solutions
- ¹⁰⁶ Laboratoire Univers et Particules de Montpellier, CNRS Université Montpellier, Place Eugène Bataillon, CC72, 34095 Montpellier Cedex 05, France
- ¹⁰⁷ Université de Caen Normandie, Côte de Nacre Boulevard Maréchal Juin, 14032 Caen, France
- ¹⁰⁸ LESIA, Observatoire de Paris, Université PSL, CNRS, Sorbonne Université, Université de Paris, 5 Place Jules Janssen, 92190 Meudon, France
- ¹⁰⁹ SRON Netherlands Institute for Space Research, Niels Bohrweg 4, 2333 CA Leiden, The Netherlands
- ¹¹⁰ Astronomical Observatory, University of Warsaw, Al. Ujazdowski 4, 00-478 Warszawa, Poland
- ¹¹¹ Scialia for CNES Centre Spatial de Toulouse, 18 avenue Edouard Belin, 31401 Toulouse Cedex 9, France
- ¹¹² Université Rennes, CNRS, IPR (Institut de Physique de Rennes) - UMR 6251, 35000 Rennes, France
- ¹¹³ INAF - Osservatorio Astronomico di Capodimonte, Via Moiarriello 16, 80131, Napoli, Italy
- ¹¹⁴ Shanghai Astronomical Observatory, Chinese Academy of Sciences, 80 Nandan Road, Shanghai 200030, People's Republic of China
- ¹¹⁵ University of Chinese Academy of Sciences, No.19(A) Yuquan Road, Shijingshan District, Beijing 100049, People's Republic of China
- ¹¹⁶ Niels Bohr Institute, University of Copenhagen, Juliane Maries Vej 30, 2100 Copenhagen Ø, Denmark
- ¹¹⁷ DXC Technology, Retortvej 8, 2500 Valby, Denmark
- ¹¹⁸ Las Cumbres Observatory, 6740 Cortona Drive Suite 102, Goleta, CA 93117, USA
- ¹¹⁹ CIGUS CITIC, Department of Nautical Sciences and Marine Engineering, University of A Coruña, Paseo de Ronda 51, 15071, A Coruña, Spain
- ¹²⁰ Astrophysics Research Institute, Liverpool John Moores University, 146 Brownlow Hill, Liverpool L3 5RF, United Kingdom
- ¹²¹ IPAC, Mail Code 100-22, California Institute of Technology, 1200 E. California Blvd., Pasadena, CA 91125, USA
- ¹²² IRAP, Université de Toulouse, CNRS, UPS, CNES, 9 Av. colonel Roche, BP 44346, 31028 Toulouse Cedex 4, France
- ¹²³ MTA CSFK Lendület Near-Field Cosmology Research Group, Konkoly Observatory, MTA Research Centre for Astronomy and Earth Sciences, Konkoly Thege Miklós út 15-17, 1121 Budapest, Hungary
- ¹²⁴ Departamento de Física de la Tierra y Astrofísica, Universidad Complutense de Madrid, 28040 Madrid, Spain
- ¹²⁵ Ruđer Bošković Institute, Bijenička cesta 54, 10000 Zagreb, Croatia

- ¹²⁶ Villanova University, Department of Astrophysics and Planetary Science, 800 E Lancaster Avenue, Villanova PA 19085, USA
- ¹²⁷ INAF - Osservatorio Astronomico di Brera, via E. Bianchi, 46, 23807 Merate (LC), Italy
- ¹²⁸ STFC, Rutherford Appleton Laboratory, Harwell, Didcot, OX11 0QX, United Kingdom
- ¹²⁹ Charles University, Faculty of Mathematics and Physics, Astronomical Institute of Charles University, V Holesovickach 2, 18000 Prague, Czech Republic
- ¹³⁰ Department of Particle Physics and Astrophysics, Weizmann Institute of Science, Rehovot 7610001, Israel
- ¹³¹ Department of Astrophysical Sciences, 4 Ivy Lane, Princeton University, Princeton NJ 08544, USA
- ¹³² Departamento de Astrofísica, Centro de Astrobiología (CSIC-INTA), ESA-ESAC. Camino Bajo del Castillo s/n. 28692 Villanueva de la Cañada, Madrid, Spain
- ¹³³ naXys, University of Namur, Rempart de la Vierge, 5000 Namur, Belgium
- ¹³⁴ CGI Deutschland B.V. & Co. KG, Mornewegstr. 30, 64293 Darmstadt, Germany
- ¹³⁵ Institute of Global Health, University of Geneva
- ¹³⁶ Astronomical Observatory Institute, Faculty of Physics, Adam Mickiewicz University, Poznań, Poland
- ¹³⁷ H H Wills Physics Laboratory, University of Bristol, Tyndall Avenue, Bristol BS8 1TL, United Kingdom
- ¹³⁸ Department of Physics and Astronomy G. Galilei, University of Padova, Vicolo dell'Osservatorio 3, 35122, Padova, Italy
- ¹³⁹ CERN, Geneva, Switzerland
- ¹⁴⁰ Applied Physics Department, Universidade de Vigo, 36310 Vigo, Spain
- ¹⁴¹ Association of Universities for Research in Astronomy, 1331 Pennsylvania Ave. NW, Washington, DC 20004, USA
- ¹⁴² European Southern Observatory, Alonso de Córdova 3107, Casilla 19, Santiago, Chile
- ¹⁴³ Sorbonne Université, CNRS, UMR7095, Institut d'Astrophysique de Paris, 98bis bd. Arago, 75014 Paris, France
- ¹⁴⁴ Faculty of Mathematics and Physics, University of Ljubljana, Jadranska ulica 19, 1000 Ljubljana, Slovenia

Acknowledgements

This work presents results from the European Space Agency (ESA) space mission *Gaia*. *Gaia* data are being processed by the *Gaia* Data Processing and Analysis Consortium (DPAC). Funding for the DPAC is provided by national institutions, in particular the institutions participating in the *Gaia* MultiLateral Agreement (MLA). The *Gaia* mission website is at <https://www.cosmos.esa.int/gaia>. The *Gaia* archive website is <https://archives.esac.esa.int/gaia>.

The *Gaia* mission and data processing have financially been supported by, in alphabetical order by country:

- the Algerian Centre de Recherche en Astronomie, Astrophysique et Géophysique of Bouzareah Observatory;
- the Austrian Fonds zur Förderung der wissenschaftlichen Forschung (FWF) Hertha Firnberg Programme through grants T359, P20046, and P23737;
- the BELgian federal Science Policy Office (BEL-SPO) through various PROgramme de Développement d’Expériences scientifiques (PRODEX) grants and the Polish Academy of Sciences - Fonds Wetenschappelijk Onderzoek through grant VS.091.16N, and the Fonds de la Recherche Scientifique (FNRS), and the Research Council of Katholieke Universiteit (KU) Leuven through grant C16/18/005 (Pushing AsteroSeismology to the next level with TESS, GaiA, and the Sloan Digital Sky SurVEy – PARADISE);
- the Brazil-France exchange programmes Fundação de Amparo à Pesquisa do Estado de São Paulo (FAPESP) and Coordenação de Aperfeiçoamento de Pessoal de Nível Superior (CAPES) - Comité Français d’Evaluation de la Coopération Universitaire et Scientifique avec le Brésil (COFECUB);
- the Chilean Agencia Nacional de Investigación y Desarrollo (ANID) through Fondo Nacional de Desarrollo Científico y Tecnológico (FONDECYT) Regular Project 1210992 (L. Chemin);
- the National Natural Science Foundation of China (NSFC) through grants 11573054, 11703065, and 12173069, the China Scholarship Council through grant 201806040200, and the Natural Science Foundation of Shanghai through grant 21ZR1474100;
- the Tenure Track Pilot Programme of the Croatian Science Foundation and the École Polytechnique Fédérale de Lausanne and the project TTP-2018-07-1171 ‘Mining the Variable Sky’, with the funds of the Croatian-Swiss Research Programme;
- the Czech-Republic Ministry of Education, Youth, and Sports through grant LG 15010 and INTER-EXCELLENCE grant LTAUSA18093, and the Czech Space Office through ESA PECS contract 98058;
- the Danish Ministry of Science;
- the Estonian Ministry of Education and Research through grant IUT40-1;
- the European Commission’s Sixth Framework Programme through the European Leadership in Space Astrometry (ELSA) Marie Curie Research Training Network (MRTN-CT-2006-033481), through Marie Curie project PIOF-GA-2009-255267 (Space AsteroSeismology & RR Lyrae stars, SAS-RRL), and through a Marie Curie Transfer-of-Knowledge (ToK) fellowship (MTKD-CT-2004-014188); the European Commission’s Seventh Framework Programme through grant FP7-606740 (FP7-SPACE-2013-1) for the *Gaia* European Network for Improved data User Services (GENIUS) and through grant 264895 for the *Gaia* Research for European Astronomy Training (GREAT-ITN) network;
- the European Cooperation in Science and Technology (COST) through COST Action CA18104 ‘Revealing the Milky Way with *Gaia* (MW-Gaia)’;
- the European Research Council (ERC) through grants 320360, 647208, and 834148 and through the European Union’s Horizon 2020 research and innovation and excellent science programmes through Marie Skłodowska-Curie grant 745617 (Our Galaxy at full HD – Gal-HD) and 895174 (The build-up and fate of self-gravitating systems in the Universe) as well as grants 687378 (Small Bodies: Near and Far), 682115 (Using the Magellanic Clouds to Understand the Interaction of Galaxies), 695099 (A sub-percent distance scale from binaries and Cepheids – CepBin), 716155 (Structured ACCREtion Disks – SACCRED), 951549 (Sub-percent calibration of the extragalactic distance scale in the era of big surveys – UniverScale), and 101004214 (Innovative Scientific Data Exploration and Exploitation Applications for Space Sciences – EXPLORE);
- the European Science Foundation (ESF), in the framework of the *Gaia* Research for European Astronomy Training Research Network Programme (GREAT-ESF);
- the European Space Agency (ESA) in the framework of the *Gaia* project, through the Plan for European Cooperating States (PECS) programme through contracts C98090 and 4000106398/12/NL/KML for Hungary, through contract 4000115263/15/NL/IB for Germany, and through Programme de Développement d’Expériences scientifiques (PRODEX) grant 4000127986 for Slovenia;
- the Academy of Finland through grants 299543, 307157, 325805, 328654, 336546, and 345115 and the Magnus Ehrnrooth Foundation;
- the French Centre National d’Études Spatiales (CNES), the Agence Nationale de la Recherche (ANR) through grant ANR-10-IDEX-0001-02 for the ‘Investissements d’avenir’ programme, through grant ANR-15-CE31-0007 for project ‘Modelling the Milky Way in the *Gaia* era’ (MOD4Gaia), through grant ANR-14-CE33-0014-01 for project ‘The Milky Way disc formation in the *Gaia* era’ (ARCHEOGAL), through grant ANR-15-CE31-0012-01 for project ‘Unlocking the potential of Cepheids as primary distance calibrators’ (UnlockCepheids), through grant ANR-19-CE31-0017 for project ‘Secular evolution of galaxies’ (SEGAL), and through grant ANR-18-CE31-0006 for project ‘Galactic Dark Matter’ (GaDaMa), the Centre National de la Recherche Scientifique (CNRS) and its SNO *Gaia* of the Institut des Sciences de l’Univers (INSU), its Programmes Nationaux: Cosmologie et Galaxies (PNCG), Gravitation Références Astronomie Métrologie (PNGRAM), Planétologie (PNP), Physique et Chimie du Milieu Interstellaire (PCMI), and Physique Stellaire (PNPS), the ‘Action Fédératrice *Gaia*’ of the Observatoire de Paris, the Région de Franche-Comté, the Institut National Polytechnique (INP) and the Institut National de Physique nucléaire et de Physique des Particules (IN2P3) co-funded by CNES;
- the German Aerospace Agency (Deutsches Zentrum für Luft- und Raumfahrt e.V., DLR) through grants 50QG0501, 50QG0601, 50QG0602, 50QG0701, 50QG0901, 50QG1001, 50QG1101, 50QG1401, 50QG1402, 50QG1403, 50QG1404, 50QG1904, 50QG2101, 50QG2102, and 50QG2202, and the Centre for Information Services and High Performance Computing (ZIH) at

- the Technische Universität Dresden for generous allocations of computer time;
- the Hungarian Academy of Sciences through the Lendület Programme grants LP2014-17 and LP2018-7 and the Hungarian National Research, Development, and Innovation Office (NKFIH) through grant KKP-137523 (‘SeismoLab’);
 - the Science Foundation Ireland (SFI) through a Royal Society - SFI University Research Fellowship (M. Fraser);
 - the Israel Ministry of Science and Technology through grant 3-18143 and the Tel Aviv University Center for Artificial Intelligence and Data Science (TAD) through a grant;
 - the Agenzia Spaziale Italiana (ASI) through contracts I/037/08/0, I/058/10/0, 2014-025-R.0, 2014-025-R.1.2015, and 2018-24-HH.0 to the Italian Istituto Nazionale di Astrofisica (INAF), contract 2014-049-R.0/1/2 to INAF for the Space Science Data Centre (SSDC, formerly known as the ASI Science Data Center, ASDC), contracts I/008/10/0, 2013/030/I.0, 2013-030-I.0.1-2015, and 2016-17-I.0 to the Aerospace Logistics Technology Engineering Company (ALTEC S.p.A.), INAF, and the Italian Ministry of Education, University, and Research (Ministero dell’Istruzione, dell’Università e della Ricerca) through the Premiale project ‘Mining The Cosmos Big Data and Innovative Italian Technology for Frontier Astrophysics and Cosmology’ (MITiC);
 - the Netherlands Organisation for Scientific Research (NWO) through grant NWO-M-614.061.414, through a VICI grant (A. Helmi), and through a Spinoza prize (A. Helmi), and the Netherlands Research School for Astronomy (NOVA);
 - the Polish National Science Centre through HARMONIA grant 2018/30/M/ST9/00311 and DAINA grant 2017/27/L/ST9/03221 and the Ministry of Science and Higher Education (MNiSW) through grant DIR/WK/2018/12;
 - the Portuguese Fundação para a Ciência e a Tecnologia (FCT) through national funds, grants SFRH/BD/128840/2017 and PTDC/FIS-AST/30389/2017, and work contract DL 57/2016/CP1364/CT0006, the Fundo Europeu de Desenvolvimento Regional (FEDER) through grant POCI-01-0145-FEDER-030389 and its Programa Operacional Competitividade e Internacionalização (COMPETE2020) through grants UIDB/04434/2020 and UIDP/04434/2020, and the Strategic Programme UIDB/00099/2020 for the Centro de Astrofísica e Gravitação (CENTRA);
 - the Slovenian Research Agency through grant P1-0188;
 - the Spanish Ministry of Economy (MINECO/FEDER, UE), the Spanish Ministry of Science and Innovation (MICIN), the Spanish Ministry of Education, Culture, and Sports, and the Spanish Government through grants BES-2016-078499, BES-2017-083126, BES-C-2017-0085, ESP2016-80079-C2-1-R, ESP2016-80079-C2-2-R, FPU16/03827, PDC2021-121059-C22, RTI2018-095076-B-C22, and TIN2015-65316-P (‘Computación de Altas Prestaciones VII’), the Juan de la Cierva Incorporación Programme (FJCI-2015-2671 and IJC2019-04862-I for F. Anders), the Severo Ochoa Centre of Excellence Programme (SEV2015-0493), and MICIN/AEI/10.13039/501100011033 (and the European Union through European Regional Development Fund ‘A way of making Europe’) through grant RTI2018-095076-B-C21, the Institute of Cosmos Sciences University of Barcelona (ICCUB, Unidad de Excelencia ‘María de Maeztu’) through grant CEX2019-000918-M, the University of Barcelona’s official doctoral programme for the development of an R+D+i project through an Ajuts de Personal Investigador en Formació (APIF) grant, the Spanish Virtual Observatory through project AyA2017-84089, the Galician Regional Government, Xunta de Galicia, through grants ED431B-2021/36, ED481A-2019/155, and ED481A-2021/296, the Centro de Investigación en Tecnologías de la Información y las Comunicaciones (CITIC), funded by the Xunta de Galicia and the European Union (European Regional Development Fund – Galicia 2014-2020 Programme), through grant ED431G-2019/01, the Red Española de Supercomputación (RES) computer resources at MareNostrum, the Barcelona Supercomputing Centre - Centro Nacional de Supercomputación (BSC-CNS) through activities AECT-2017-2-0002, AECT-2017-3-0006, AECT-2018-1-0017, AECT-2018-2-0013, AECT-2018-3-0011, AECT-2019-1-0010, AECT-2019-2-0014, AECT-2019-3-0003, AECT-2020-1-0004, and DATA-2020-1-0010, the Departament d’Innovació, Universitats i Empresa de la Generalitat de Catalunya through grant 2014-SGR-1051 for project ‘Models de Programació i Entorns d’Execució Paralels’ (MPEXPAN), and Ramon y Cajal Fellowship RYC2018-025968-I funded by MICIN/AEI/10.13039/501100011033 and the European Science Foundation (‘Investing in your future’);
 - the Swedish National Space Agency (SNSA/Rymdstyrelsen);
 - the Swiss State Secretariat for Education, Research, and Innovation through the Swiss Activités Nationales Complémentaires and the Swiss National Science Foundation through an Eccellenza Professorial Fellowship (award PCEFP2_194638 for R. Anderson);
 - the United Kingdom Particle Physics and Astronomy Research Council (PPARC), the United Kingdom Science and Technology Facilities Council (STFC), and the United Kingdom Space Agency (UKSA) through the following grants to the University of Bristol, the University of Cambridge, the University of Edinburgh, the University of Leicester, the Mullard Space Sciences Laboratory of University College London, and the United Kingdom Rutherford Appleton Laboratory (RAL): PP/D006511/1, PP/D006546/1, PP/D006570/1, ST/I000852/1, ST/J005045/1, ST/K00056X/1, ST/K000209/1, ST/K000756/1, ST/L006561/1, ST/N000595/1, ST/N000641/1, ST/N000978/1, ST/N001117/1, ST/S000089/1, ST/S000976/1, ST/S000984/1, ST/S001123/1, ST/S001948/1, ST/S001980/1, ST/S002103/1, ST/V000969/1, ST/W002469/1, ST/W002493/1, ST/W002671/1, ST/W002809/1, and EP/V520342/1.
- The *Gaia* project and data processing have made use of:
- the Set of Identifications, Measurements, and Bibliography for Astronomical Data (SIMBAD, Wenger et al. 2000), the ‘Aladin sky atlas’ (Bonnarel et al. 2000; Boch & Fernique 2014), and the VizieR catalogue access tool (Ochsenbein et al. 2000), all operated at the Centre de Données astronomiques de Strasbourg (CDS);
 - the National Aeronautics and Space Administration (NASA) Astrophysics Data System (ADS);
 - the SPace ENVIRONMENT Information System (SPENVIS), initiated by the Space Environment and Effects Section (TEC-EES) of ESA and developed by the Belgian Institute for Space Aeronomy (BIRA-IASB) under ESA contract through ESA’s General Support Technologies Programme (GSTP), administered by the BELgian federal Science Policy Office (BELSPO);

- the software products TOPCAT, STIL, and STILTS (Taylor 2005a, 2006);
- Matplotlib (Hunter 2007);
- IPython (Pérez & Granger 2007);
- Astropy, a community-developed core Python package for Astronomy (Astropy Collaboration et al. 2018);
- R (R Core Team 2013);
- Vaex (Breddels & Veljanoski 2018);
- the Hipparcos-2 catalogue (van Leeuwen 2007). The Hipparcos and Tycho catalogues were constructed under the responsibility of large scientific teams collaborating with ESA. The Consortia Leaders were Lennart Lindegren (Lund, Sweden: NDAC) and Jean Kovalevsky (Grasse, France: FAST), together responsible for the Hipparcos Catalogue; Erik Høg (Copenhagen, Denmark: TDAC) responsible for the Tycho Catalogue; and Catherine Turon (Meudon, France: INCA) responsible for the Hipparcos Input Catalogue (HIC);
- the Tycho-2 catalogue (Høg et al. 2000), the construction of which was supported by the Velux Foundation of 1981 and the Danish Space Board;
- The Tycho double star catalogue (TDSC, Fabricius et al. 2002), based on observations made with the ESA Hipparcos astrometry satellite, as supported by the Danish Space Board and the United States Naval Observatory through their double-star programme;
- data products from the Two Micron All Sky Survey (2MASS, Skrutskie et al. 2006), which is a joint project of the University of Massachusetts and the Infrared Processing and Analysis Center (IPAC) / California Institute of Technology, funded by the National Aeronautics and Space Administration (NASA) and the National Science Foundation (NSF) of the USA;
- the ninth data release of the AAVSO Photometric All-Sky Survey (APASS, Henden et al. 2016), funded by the Robert Martin Ayers Sciences Fund;
- the first data release of the Pan-STARRS survey (Chambers et al. 2016; Magnier et al. 2020a; Waters et al. 2020; Magnier et al. 2020c,b; Flewelling et al. 2020). The Pan-STARRS1 Surveys (PS1) and the PS1 public science archive have been made possible through contributions by the Institute for Astronomy, the University of Hawaii, the Pan-STARRS Project Office, the Max-Planck Society and its participating institutes, the Max Planck Institute for Astronomy, Heidelberg and the Max Planck Institute for Extraterrestrial Physics, Garching, The Johns Hopkins University, Durham University, the University of Edinburgh, the Queen’s University Belfast, the Harvard-Smithsonian Center for Astrophysics, the Las Cumbres Observatory Global Telescope Network Incorporated, the National Central University of Taiwan, the Space Telescope Science Institute, the National Aeronautics and Space Administration (NASA) through grant NNX08AR22G issued through the Planetary Science Division of the NASA Science Mission Directorate, the National Science Foundation through grant AST-1238877, the University of Maryland, Eotvos Lorand University (ELTE), the Los Alamos National Laboratory, and the Gordon and Betty Moore Foundation;
- the second release of the Guide Star Catalogue (GSC2.3, Lasker et al. 2008). The Guide Star Catalogue II is a joint project of the Space Telescope Science Institute (STScI) and the Osservatorio Astrofisico di Torino (OATo). STScI is operated by the Association of Universities for Research in Astronomy (AURA), for the National Aeronautics and Space Administration (NASA) under contract NAS5-26555. OATo is operated by the Italian National Institute for Astrophysics (INAF). Additional support was provided by the European Southern Observatory (ESO), the Space Telescope European Coordinating Facility (STECF), the International GEMINI project, and the European Space Agency (ESA) Astrophysics Division (nowadays SCI-S);
- the eXtended, Large (XL) version of the catalogue of Positions and Proper Motions (PPM-XL, Roeser et al. 2010);
- data products from the Wide-field Infrared Survey Explorer (WISE), which is a joint project of the University of California, Los Angeles, and the Jet Propulsion Laboratory/California Institute of Technology, and NEOWISE, which is a project of the Jet Propulsion Laboratory/California Institute of Technology. WISE and NEOWISE are funded by the National Aeronautics and Space Administration (NASA);
- the first data release of the United States Naval Observatory (USNO) Robotic Astrometric Telescope (URAT-1, Zacharias et al. 2015);
- the fourth data release of the United States Naval Observatory (USNO) CCD Astrograph Catalogue (UCAC-4, Zacharias et al. 2013);
- the sixth and final data release of the Radial Velocity Experiment (RAVE DR6, Steinmetz et al. 2020a,b). Funding for RAVE has been provided by the Leibniz Institute for Astrophysics Potsdam (AIP), the Australian Astronomical Observatory, the Australian National University, the Australian Research Council, the French National Research Agency, the German Research Foundation (SPP 1177 and SFB 881), the European Research Council (ERC-StG 240271 Galactica), the Istituto Nazionale di Astrofisica at Padova, the Johns Hopkins University, the National Science Foundation of the USA (AST-0908326), the W.M. Keck foundation, the Macquarie University, the Netherlands Research School for Astronomy, the Natural Sciences and Engineering Research Council of Canada, the Slovenian Research Agency, the Swiss National Science Foundation, the Science & Technology Facilities Council of the UK, Opticon, Strasbourg Observatory, and the Universities of Basel, Groningen, Heidelberg, and Sydney. The RAVE website is at <https://www.rave-survey.org/>;
- the first data release of the Large sky Area Multi-Object Fibre Spectroscopic Telescope (LAMOST DR1, Luo et al. 2015);
- the K2 Ecliptic Plane Input Catalogue (EPIC, Huber et al. 2016);
- the ninth data release of the Sloan Digital Sky Survey (SDSS DR9, Ahn et al. 2012). Funding for SDSS-III has been provided by the Alfred P. Sloan Foundation, the Participating Institutions, the National Science Foundation, and the United States Department of Energy Office of Science. The SDSS-III website is <http://www.sdss3.org/>. SDSS-III is managed by the Astrophysical Research Consortium for the Participating Institutions of the SDSS-III Collaboration including the University of Arizona, the Brazilian Participation Group, Brookhaven National Laboratory, Carnegie Mellon University, University of Florida, the French Participation Group, the German Participation Group, Harvard University, the Instituto de Astrofísica de Canarias, the Michigan State/Notre Dame/JINA Participation Group, Johns Hopkins University, Lawrence Berkeley National Laboratory, Max Planck Institute for Astrophysics, Max Planck Institute for Extraterrestrial Physics, New Mexico State University, New York University, Ohio State University, Pennsylvania State University, University of Portsmouth, Princeton University,

- the Spanish Participation Group, University of Tokyo, University of Utah, Vanderbilt University, University of Virginia, University of Washington, and Yale University;
- the thirteenth release of the Sloan Digital Sky Survey (SDSS DR13, Albareti et al. 2017). Funding for SDSS-IV has been provided by the Alfred P. Sloan Foundation, the United States Department of Energy Office of Science, and the Participating Institutions. SDSS-IV acknowledges support and resources from the Center for High-Performance Computing at the University of Utah. The SDSS web site is <https://www.sdss.org/>. SDSS-IV is managed by the Astrophysical Research Consortium for the Participating Institutions of the SDSS Collaboration including the Brazilian Participation Group, the Carnegie Institution for Science, Carnegie Mellon University, the Chilean Participation Group, the French Participation Group, Harvard-Smithsonian Center for Astrophysics, Instituto de Astrofísica de Canarias, The Johns Hopkins University, Kavli Institute for the Physics and Mathematics of the Universe (IPMU) / University of Tokyo, the Korean Participation Group, Lawrence Berkeley National Laboratory, Leibniz Institut für Astrophysik Potsdam (AIP), Max-Planck-Institut für Astronomie (MPIA Heidelberg), Max-Planck-Institut für Astrophysik (MPA Garching), Max-Planck-Institut für Extraterrestrische Physik (MPE), National Astronomical Observatories of China, New Mexico State University, New York University, University of Notre Dame, Observatório Nacional / MCTI, The Ohio State University, Pennsylvania State University, Shanghai Astronomical Observatory, United Kingdom Participation Group, Universidad Nacional Autónoma de México, University of Arizona, University of Colorado Boulder, University of Oxford, University of Portsmouth, University of Utah, University of Virginia, University of Washington, University of Wisconsin, Vanderbilt University, and Yale University;
 - the second release of the SkyMapper catalogue (SkyMapper DR2, Onken et al. 2019, Digital Object Identifier 10.25914/5ce60d31ce759). The national facility capability for SkyMapper has been funded through grant LE130100104 from the Australian Research Council (ARC) Linkage Infrastructure, Equipment, and Facilities (LIEF) programme, awarded to the University of Sydney, the Australian National University, Swinburne University of Technology, the University of Queensland, the University of Western Australia, the University of Melbourne, Curtin University of Technology, Monash University, and the Australian Astronomical Observatory. SkyMapper is owned and operated by The Australian National University’s Research School of Astronomy and Astrophysics. The survey data were processed and provided by the SkyMapper Team at the the Australian National University. The SkyMapper node of the All-Sky Virtual Observatory (ASVO) is hosted at the National Computational Infrastructure (NCI). Development and support the SkyMapper node of the ASVO has been funded in part by Astronomy Australia Limited (AAL) and the Australian Government through the Commonwealth’s Education Investment Fund (EIF) and National Collaborative Research Infrastructure Strategy (NCRIS), particularly the National eResearch Collaboration Tools and Resources (NeCTAR) and the Australian National Data Service Projects (ANDS);
 - the *Gaia*-ESO Public Spectroscopic Survey (GES, Gilmore et al. 2022; Randich et al. 2022). The *Gaia*-ESO Survey is based on data products from observations made with ESO Telescopes at the La Silla Paranal Observatory under programme ID 188.B-3002. Public data releases are available

through the ESO Science Portal. The project has received funding from the Leverhulme Trust (project RPG-2012-541), the European Research Council (project ERC-2012-AdG 320360-Gaia-ESO-MW), and the Istituto Nazionale di Astrofisica, INAF (2012: CRA 1.05.01.09.16; 2013: CRA 1.05.06.02.07).

The GBOT programme uses observations collected at (i) the European Organisation for Astronomical Research in the Southern Hemisphere (ESO) with the VLT Survey Telescope (VST), under ESO programmes 092.B-0165, 093.B-0236, 094.B-0181, 095.B-0046, 096.B-0162, 097.B-0304, 098.B-0030, 099.B-0034, 0100.B-0131, 0101.B-0156, 0102.B-0174, and 0103.B-0165; and (ii) the Liverpool Telescope, which is operated on the island of La Palma by Liverpool John Moores University in the Spanish Observatorio del Roque de los Muchachos of the Instituto de Astrofísica de Canarias with financial support from the United Kingdom Science and Technology Facilities Council, and (iii) telescopes of the Las Cumbres Observatory Global Telescope Network.

In case of errors or omissions, please contact the *Gaia* Helpdesk.

This work was eased by the use of the data handling and visualisation software TOPCAT (Taylor 2005b), gnuplot, python, and astropy. Auxiliary data are provided by the Minor Planet Physical Properties Catalogue ⁶ of the Observatoire de la Côte d’Azur. M. Delbo wish to thank F. DeMeo, S. Raymond, C. Avdellidou for helpful discussions and M. Galinier (DPAC / CNES / OCA) for an editorial revision of the manuscript. The authors would like to thank editorial handling by T. Forveille and J. Neve, as well as comments and constructive criticisms from an anonymous reviewer.

Appendix A: Dispersion of the photometric instrument

The figure A.1 of the nominal dispersion function of the BP and the RP is taken from the ESA website ⁷.

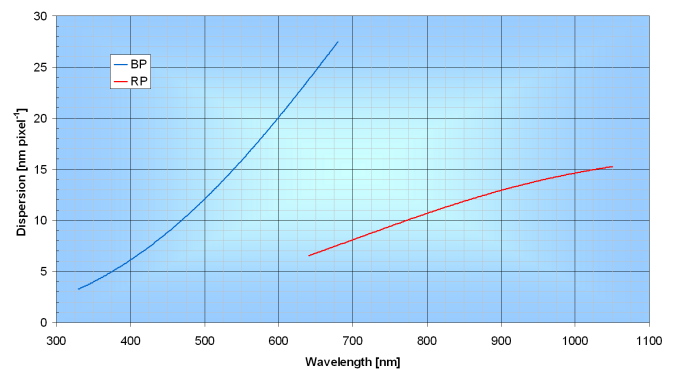


Fig. A.1. Nominal dispersion curves of the BP/RP instrument.

⁶ mp3c.oca.eu

⁷ <https://www.cosmos.esa.int/web/gaia/resolution>

Appendix B: Astronomical Data Query Language (ADQL) queries

Appendix B.1: Request of a single spectrum of an asteroid

The following query returns the wavelengths, reflectances, and reflectance errors for the asteroid (21) Lutetia.

```
SELECT wavelength, reflectance_spectrum,
reflectance_spectrum_err
FROM gaidr3.sso_reflectance_spectrum
WHERE number_mp = 21
```

The same query can be written using the designation this time. The reader should be aware that no capital letters are taken into account.

```
SELECT wavelength, reflectance_spectrum,
reflectance_spectrum_err
FROM gaidr3.sso_reflectance_spectrum
WHERE designation = 'lutetia'
```

Appendix C: Solar analogue

As shown by Cellino et al. (2020), the choice of the solar analogue used to compute the asteroid average reflectance spectrum is crucial. Depending on the spectrum of the taken solar analogue, one can observe effects on the slope or the absorption band of the resulting mean reflectance spectrum of the asteroid.

The approach for computing the average solar analogue spectrum is described below:

- We created a list of known solar analogue stars used for asteroid spectroscopy.
- We computed an average spectrum from all the spectra of the list. Namely, firstly we normalised each spectrum by dividing point to point by the sum of the fluxes of BP and RP; next we calculated the average spectra of all normalised spectra and its uncertainty.
- From visual inspection of the internally calibrated XP spectra of the sources in the list, we noted that some of them are discrepant from the general spectrum of the set.

From the ground, a series of trusted solar analogues have been used over the years. *Gaia* has observed these stars multiple times. We analysed their mean spectra and found little variation across the sample. In Table C.1, the list of solar analogue stars is detailed with information such as the magnitude and the spectral type of the corresponding stars.

The information relative to the solar analogues used in the context of asteroid spectroscopy is depicted in ESA *Gaia* DR3 auxiliary data webpage⁸.

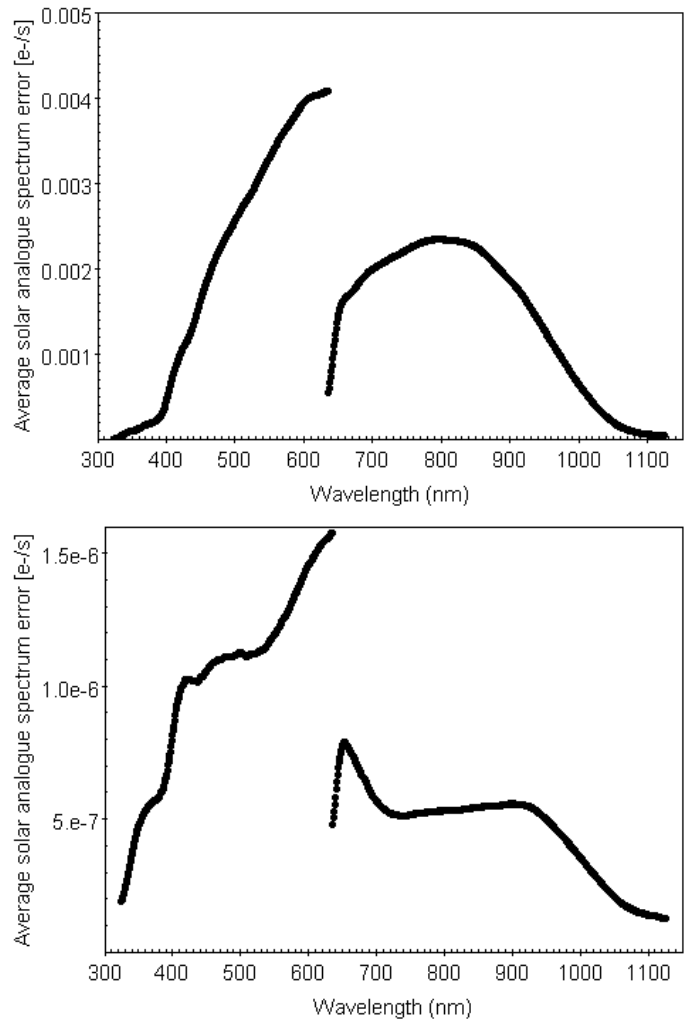


Fig. C.1. Average solar analogue spectrum computed for *Gaia* (top figure) and its error (bottom figure) are plotted. The curves with support in the wavelength range between 320 and 640 nm and between 640 and 1130 nm correspond to the BP and the RP, respectively.

⁸ <https://www.cosmos.esa.int/web/gaia/dr3-solar-analogue-spectrum>

Table C.1. Solar analogue stars selected to compute the average spectrum.

Denomination	<i>Gaia</i> DR3 sourceId	RA [°]	DEC [°]	<i>G</i>	Spectral Type	Reference
HD6400	2352876238295485440	16.178114	-20.987929	9.30	G2V	a
HD182081	4295820654469438848	290.679459	7.729991	9.39	G2V	b
HD146233	4345775217221821312	243.906303	-8.371572	5.30	G2V	c
HD20926	5103333467421759616	50.470306	-19.395128	9.64	G2V	a
HD220764	2409392888309495424	351.641401	-12.538598	9.47	G2V	d
SAO140573	4416093315142832128	232.604610	-1.318933	8.99	G3V	e
16CygB	2135550755683405952	295.452970	50.524376	5.80	G1.5V	f
SA110-361	4272476270261273216	280.687525	0.134614	12.27		g
HD220022	2385351065840541184	350.185850	-22.308895	9.54	G3V	e
HD202282	6883947988319565568	318.798564	-15.741823	8.82	G3V	a
HD16640	2502734072523738496	40.036149	2.918174	8.61	G2V	a
SAO185145	4109488347412656640	258.130251	-25.227387	8.16	G2V	e
SA107-684	4416641352970215936	234.325877	-0.163956	8.26	G2/3V	g
SAO63954	1478734360725538944	212.205186	32.949572	9.01	G0V	e
HD100044	3560743225161573120	172.653749	-15.103249	9.36	G2V	b
HD154424	5965123126448738816	256.856628	-43.837913	9.04	G2V	a
SAO41869	924370390524853120	113.817066	40.506394	7.50	G0E	e
HD144585	4341501106288171008	241.762879	-14.071255	6.14	G2V	h
SA98-978	3113329094598313472	102.890626	-0.192218	10.43	F8E	a

a. Perna et al. (2018b), b. Popescu, M. et al. (2019), c. Soubiran, C. & Triaud, A. (2004), d. Popescu, M. et al. (2014), e. Lucas et al. (2019), f. Bus & Binzel (2002b), g. Fornasier et al. (2007), h. Lazzaro et al. (2004a).

Appendix D: Colour palette code

Python example code:

The file `specParam.dat` contains the `ssoId`, the computed S/N, the spectral slope, and the `z-i` computed as explained in the corresponding session. The reader can easily recompute these data using the explanation provided in this paper.

```
import numpy as np
import matplotlib.pyplot as plt

def spec2C(slope, zi):
    b = -1./25*(slope - 20)
    b[b > 1] = 1.
    b[b < 0] = 0.

    r = 1./24*(slope + 5)
    r[r > 1] = 1.
    r[r < 0] = 0.

    g = -1./3*zi;
    g[g > 1] = 1.
    g[g < 0] = 0.

    return np.transpose(np.array([r, g, b]))

#### LOAD DATA FILES
gid, snr, slope, zi = np.loadtxt('specParam.dat',
                                usecols=(0,1,2,3), unpack=True)
a, e, sini, fam = np.loadtxt('orb_elem.dat',
                              usecols=(4,5,6,13), unpack=True)

### CALCULATE COLOURS
C = spec2C(slope, zi)
### SORT by SSO NUMBER
j = np.argsort(gid)[::-1]

### CLEAR PLOTS
plt.cla()
plt.clf()
### EXAMPLE OF PLOT
plt.scatter(a[j], sini[j], c=C[j], alpha=0.5,
            s=1.25, marker='o', edgecolors='none')
```

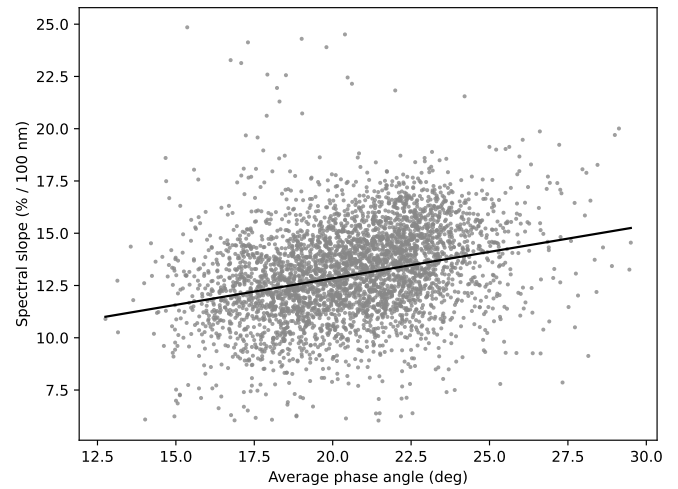
Appendix E: Phase-angle dependence of spectral parameters

Fig. E.1. Distribution of the spectral slope as a function of the mean phase angle for asteroids with $S/N > 50$ and spectral parameters within the region of the S-complex according to DeMeo & Carry (2013). The straight line is fit to the underlining distribution. See Section 4.4 for further information.

Appendix F: *Gaia* vs. SMASSII spectral parameters

We calculated spectral slope and z-i colours for the *Gaia* DR3 asteroids and those of the SMASSII⁹ and selected only those objects common to both surveys. Figure F.1 shows that the spectral slope and z-i colour differences between the two surveys, indicated by ΔS and ΔC , respectively, is a weak function of *Gaia*'s spectral slope S_{gaia} . Next, we fit a second-order polynomial to the spectral slope and z-i differences as a function of the *Gaia* spectral slope. We find that $\Delta S = 1.01532733 - 0.07180434S + 0.01156685S^2$, and $\Delta C = 0.04193216 + 0.00685427S - 0.000211S^2$.

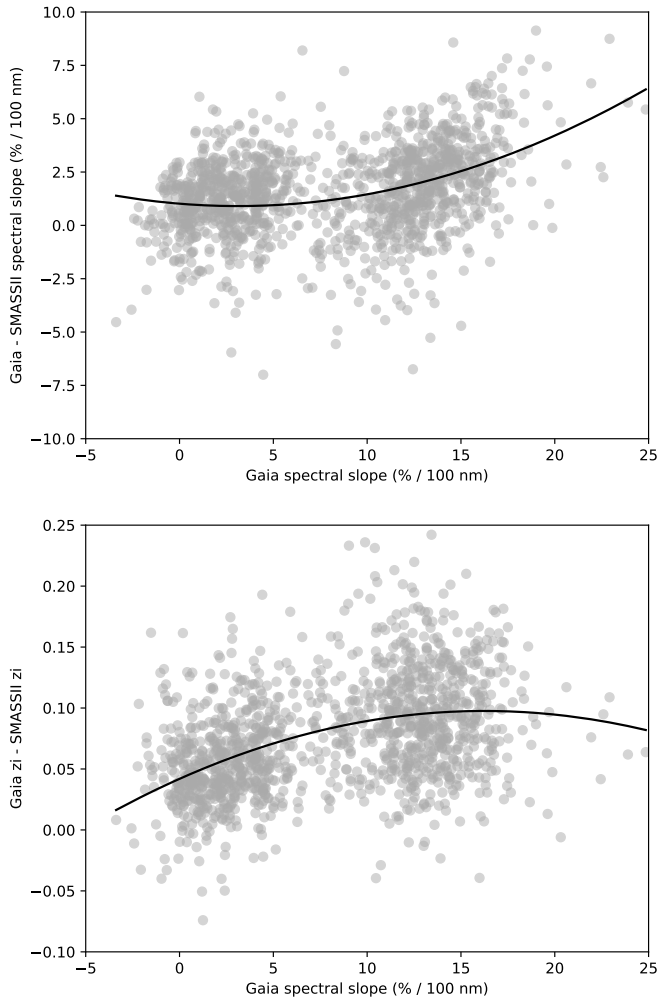


Fig. F.1. Spectral parameter difference between *Gaia* DR3 and SMASSII. Top panel: Spectral slope difference. Bottom panel: z-i colour difference. Grey circles are the data, whereas the solid lines represent the second-order polynomial fit to the data (see Section 4.2).

Appendix G: Plots comparing *Gaia* spectra to ground-based literature

In this Appendix we add all the comparative plots (see Figures G.1 and G.2) of *Gaia* mean reflectance spectra and the literature ground-based spectra discussed in Section 4.2.

⁹ <http://smass.mit.edu>

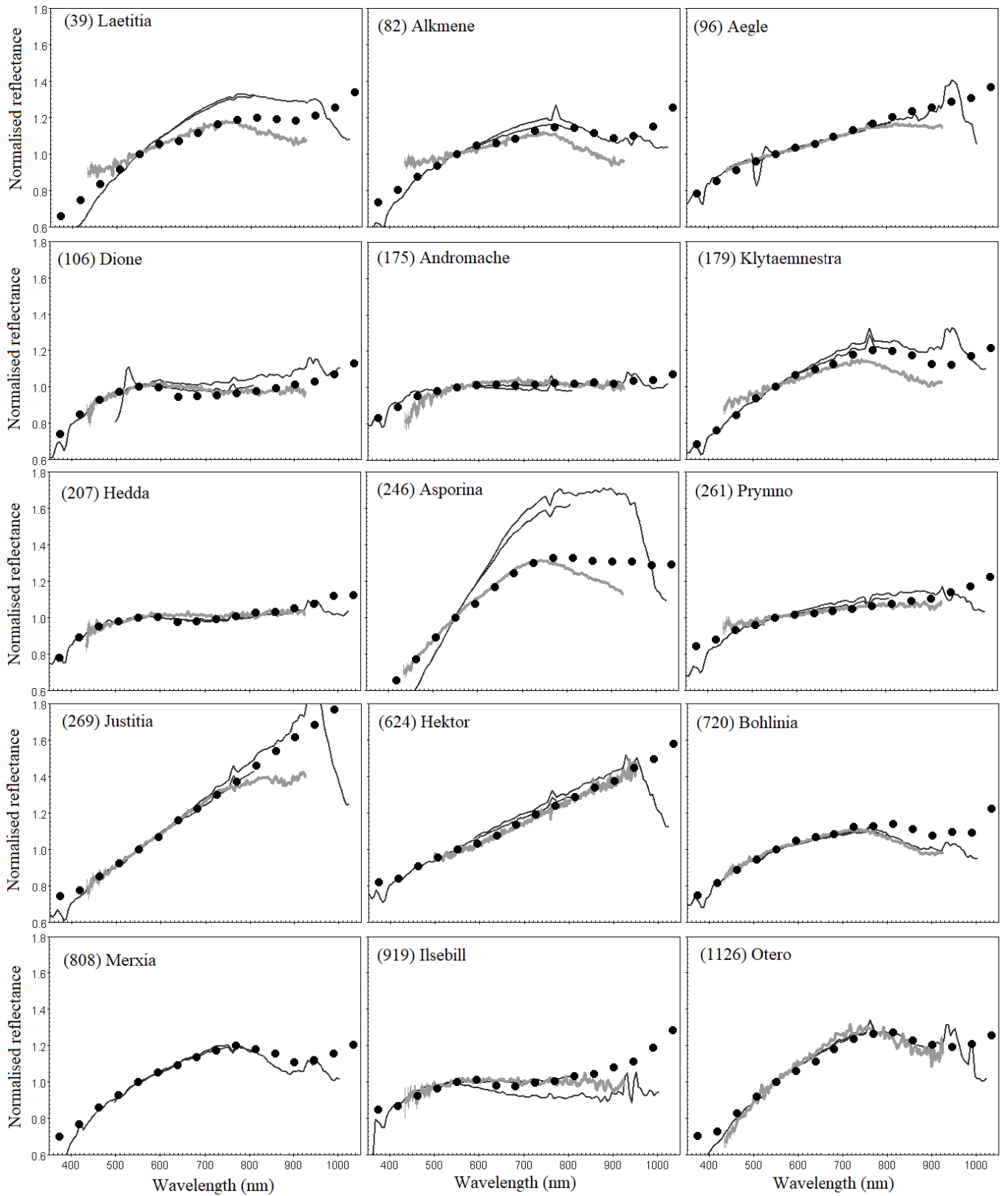


Fig. G.1. *Gaia*'s mean reflectance spectra (black circles) against ground-based observations; Cellino et al. (2020) spectra in dark grey lines and in light grey lines for asteroids (624) (Vilas et al. 1993) and (39), (82), (96), (106), (207), (246), (261), (269), (720), (919), (1126) (Bus & Binzel 2002b).

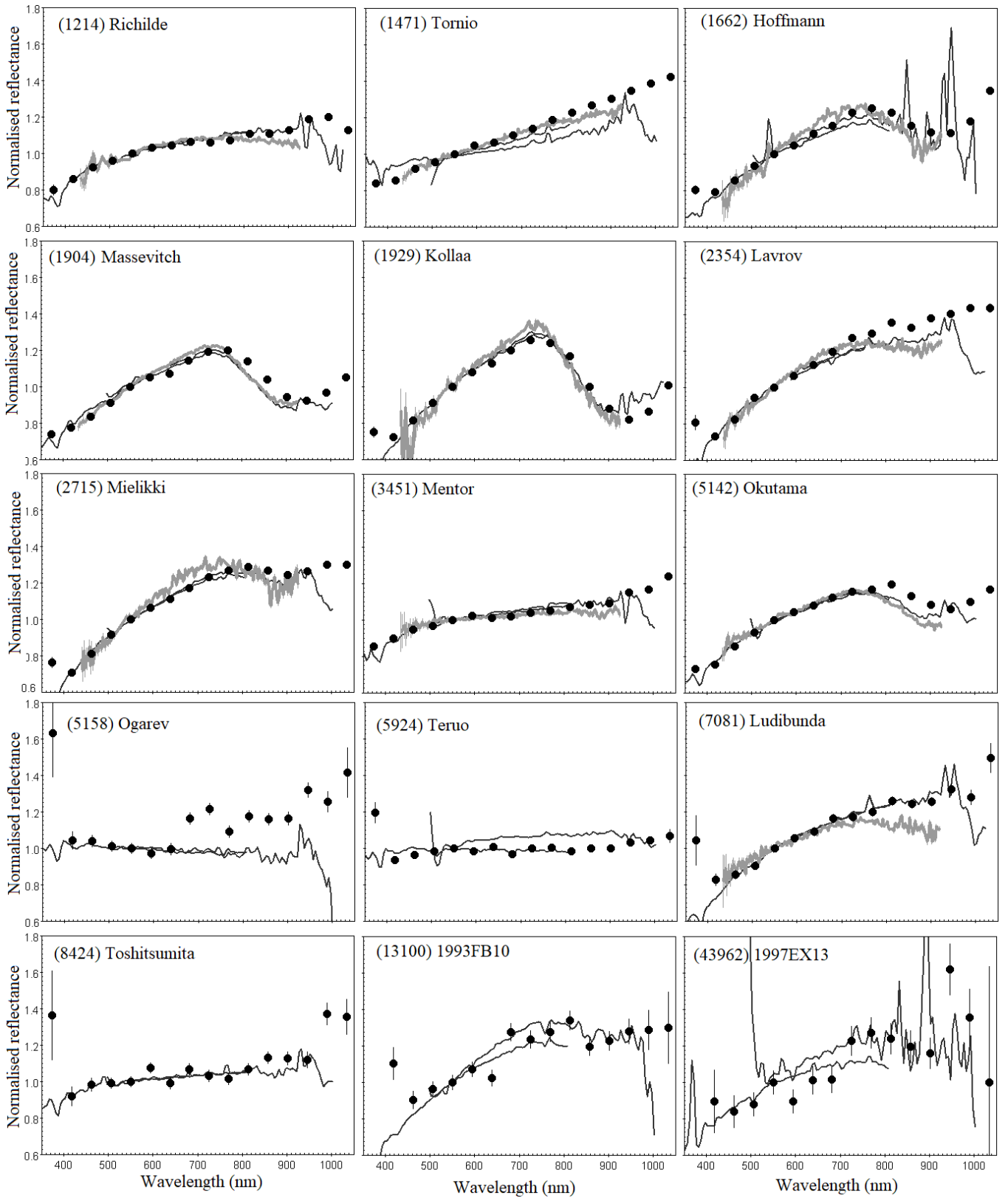


Fig. G.2. *Gaia*'s mean reflectance spectra (black circles) against ground-based observations; Cellino et al. (2020) spectra in dark grey lines and those of (Bus & Binzel 2002b) in light grey lines for asteroids (1214), (1471), (1662), (1904), (2354), (2715), (3451), (5142), (7081).